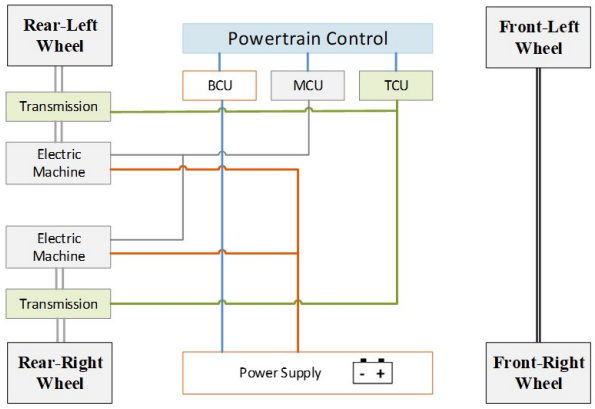

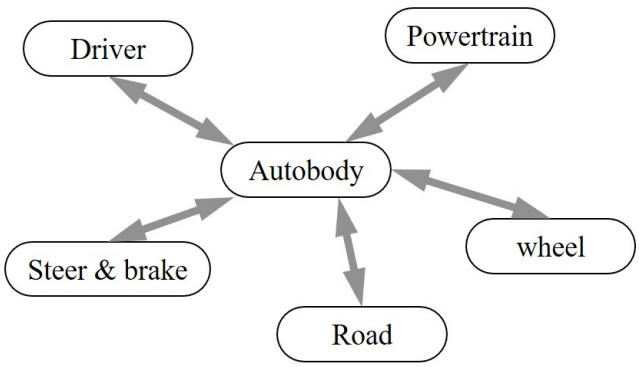

Multi-motor Control and Efficiency Optimization for Distributed Drive EV System

Master's thesis in Electrical Power Engineering

CHUAN LI

DEPARTMENT OF ELECTRICAL ENGINEERING
CHALMERS UNIVERSITY OF TECHNOLOGY
Gothenburg, Sweden 2021

Master's thesis 2021

Multi-motor Control and Efficiency Optimization for Distributed Drive EV System

CHUAN LI

CHALMERS
UNIVERSITY OF TECHNOLOGY

Department of Electrical Engineering
Chalmers University of Technology
Gothenburg, Sweden 2021

Multi-motor Control and Efficiency Optimization for
Distributed Drive EV System
CHUAN LI

Supervisors:
Xiaoliang Huang, Chalmers University of Technology
Bowen Jiang, Chalmers University of Technology
Nimananda Sharma, Chalmers University of Technology

Examiner:
Yujing Liu, Chalmers University of Technology

Typeset in LATEX
Printed by Chalmers University of Technology
Gothenburg, Sweden 2021

Multi-motor Control and Efficiency Optimization for
Distributed Drive EV System
CHUAN LI
Program of Electrical Power Engineering (MPEPO)

Abstract

The energy efficiency of electric vehicles (EVs) is arguably the most critical factor in their acceptance in today's market. As a result, a great deal of research on EVs is motivated by the prospect of improving energy efficiency.

The purpose of this thesis is to study the high-fidelity vehicle modeling approach and its multi-functionalities. The co-simulation approach combines electric powertrain system of electric machine, inverter, gearbox with high-fidelity vehicle models of driver, steer brake, autobody wheel, and road environment. Different coupling methods and comparison between vehicle and electric powertrain system are introduced. These methods pave the way for the further research of real-time simulation platform and hardware-in-the-loop (HIL) test bench.

The proposed co-simulation platform supports the feasibility of interactions with various subsystems like thermal model, wheel slip control model, and different electric machines. Coupling lumped parameter thermal networks to simulate heat dissipation in electric machine and inverter are also presented. The aim is to demonstrate versatility of the co-simulation method in estimating temperatures in devices under various driving conditions. And the simulation of thermal dynamics with different driver behaviors are studied. Furthermore, the functionalities of a wheel slip control method during acceleration and braking are also tested in this platform. The simulation results support the feasibility of this controller in further research.

Keywords: Electric vehicle, electric powertrain, Co-simulation, thermal analysis, Wheel slip control, high-fidelity modeling.

Acknowledgements

I would first like to thank IPG CarMaker Corporation together with Chalmers University of Technology for giving me the opportunity to perform the study leading up to this thesis report.

I would also like to thank Shreyas Kogalur and David Gosert at IPG CarMaker Corporation for interesting discussions and support during this thesis.

Most of all I would like to express my gratitude to Bowen Jiang, Nimananda Sharma, Xiaoliang Huang and Yujing Liu at Chalmers for the useful comments, remarks and engagements through the learning process of this master thesis

Finally, I must express my profound gratitude to my parents for providing me with unfailing support and continuous encouragement throughout my years of study. This accomplishment would not have been possible without them. Thank you.

Chuan Li, Gothenburg, Sweden, June 2021

Contents

1

Introduction

1.1 Problem Background

The energy efficiency of electric vehicles (EVs) is arguably the most critical factor in their acceptance in today's market. As a result, a great deal of research on EVs is motivated by the prospect of improving energy efficiency [1, 4]. Model-based and simulation-based optimizations have been a major part of the research, leading to the development of various simulation platforms, such as CarMaker [5], Carsim [6], ADAMS [7], etc. CarMaker, for example, includes a complete model environment including an intelligent driver model, a detailed vehicle model and a highly flexible road and traffic model based on MATLAB/Simulink platform[8], which can be satisfied for most research needs. While in electric models like powertrain, CarMaker and other tools are using the look-up table based efficiency maps to do the simulation, therefore, dynamics of voltage, current, and impacts of machine controllers are not observable. And these values are important for the efficiency optimization in electric vehicle[9].

On the other hand, various physics-based models are often used for subcomponents analysis. For example, finite-element method (FEM) models of electric machines [10], Spice models of power electronics [11], and electrochemical models of batteries [12]. They probably are good for each component but unsuitable for system studies. Therefore, the need for considering the real-world conditions during calculation has encouraged system-level simulation of vehicles by coupling with high-fidelity subcomponents such as electrical powertrain, mechanical transmission, and thermal models [13, 16]. For example, time-stepped FEM and field-circuit co-simulation strategies were used to analyse a fault-tolerant permanent magnet machine for an electric vehicle [17]. In [18], a finite element model of the motor in Maxwell was coupled to an inverter model in Simplorer to validate a flux weakening control strategy. Although these co-simulation methods can be used to study certain system-level phenomena, their computational resource requirements and the complexity of their interfaces make them unsuitable for use in full vehicle simulations.

Mathematical models [19], using lumped parameters and differential equations, can be used to address the above challenges. Firstly, the lumped parameter representation simplifies the model and thus reducing computation load compared to physics-based models. Secondly, since such models can be easily implemented in a common environment, defining signal interfaces between subsystem models will

take less effort [20]. Therefore, it is valuable to do some research on high-fidelity vehicle modeling by co-simulation approach. To validate the multi-functions of proposed high-fidelity vehicle platform, two thermal models of electric machine and inverter [21, 23], and a wheel slip control model are also introduced. Fig.1.1 shows the flowchart of co-simulation between vehicle and electric powertrain system.

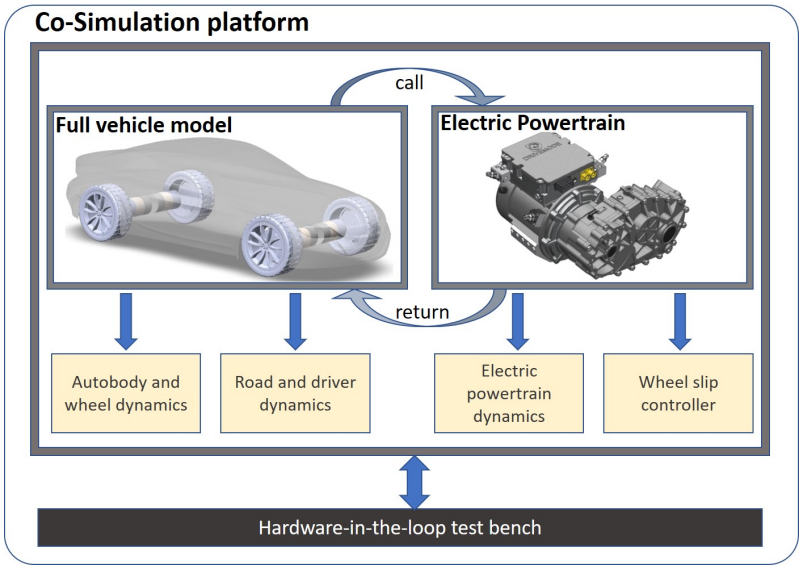

Figure 1.1: The flowchart of co-simulation between vehicle and electric powertrain

This research is also involved and founded by the Europe DRIVEMODE project. The DRIVEMODE project is a joint venture funded by the EU to develop the next generation of electric powertrains for the automotive industry [24]. Until now, most battery electric vehicles have had drivetrains featuring electric motors running at a maximum speed of 15,000 rpm, corresponding to a gear ratio of approximately 10:1. In DRIVEMODE we aim to push the input speed to an input speed of 20,000 rpm with a gear ratio of 14.1:1. The DRIVEMODE traction power system combines with a frequency converter, motor and gearbox as shown in Fig.1.2. are tightly integrated to suit each other's parameters . and are united by a single cooling circuit and frame. Large-scale manufacturing of integrated drive trains is achieved through modularity. The modular driveline concept developed is suitable for both low and high-performance vehicles.

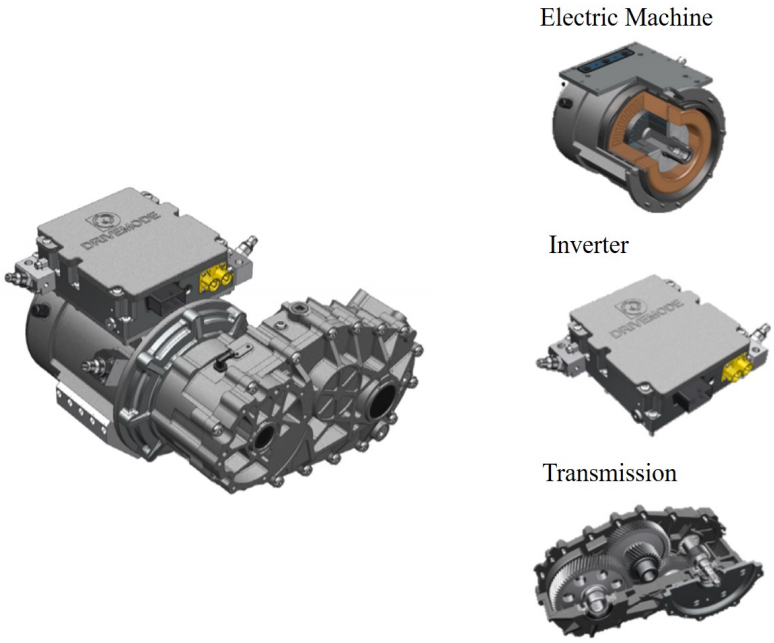

Figure 1.2: The modular structure of DRIVEMODE electric powertrain

1.2 Thesis Purpose

The objective of this thesis is to study the co-simulation approach by combing mathematical models of electric powertrain and vehicle. The electric powertrain system consists of electric machine, inverter and transmission, which is implemented with PLECS tool. The mathematical description of electric machine contains incremental inductance and apparent inductance mode. The electric vehicle consisting of driver, steer brake, autobody, wheel, road and environment is modeled by CarMaker. Both PLECS and CarMaker can be established into the Simulink Environment.

The simulation method provides access to vehicle and electric powertrain variables such as traction torque, wheel slip, phase currents of electric machine, DC link voltage, etc. Subsystem performance can therefore be investigated under various driving conditions and vice versa using the proposed method. The coupling method between vehicle and electric powertrain consists of torque open-loop, torque close-loop, speed open-loop, and speed close-loop.

Another aim of this paper is to analyze influences of driver behaviors on thermal performance of electric machine and inverter. So, lumped parameter thermal networks (LPTNs) representing heat dissipation in electric machine and inverter are also modeled to observe the temperatures of electric machine windings and semiconductor junctions. Moreover, this platform also validates a wheel slip control under different driving conditions, and the brief introduction of wheel slip control method is also presented in vehicle modeling.

The main objectives can be grouped into:

- Building the electric powertrain model, including electric machine, inverter, and transmission, and thermal model under offline PLECS/Simulink environment.

- Introduce the electric vehicle modeling with autobody wheel, steer brake, driver, road, environment, and wheel slip control units based on CarMaker/Simulink software.

- Study the different coupling methods between vehicle model and electric powertrain model.

- Four cases study to shows the multi-functional property of co-simulation vehicle model.

1.3 Limitations

- In high-fidelity vehicle modeling, the offline CarMaker/PLECS co-simulation normally is not suitable for validations. Because it remains a trade-off issue between models complexity and running speed. i.e., Higher precision models consumes large amount of time. So, this platform is only used to verify the feasibility of co-simulation.

- The purpose of this thesis is focusing on high-fidelity vehicle modeling. Only the simplified thermal model study and wheel slip control are considered. The thermal model and wheel slip control model are still not suitable for high-precision research, but these can be achieved by deeper research based on the proposed platform.

2

Electric Powertrain Modeling

The detailed electric powertrain system consists of electric machine, inverter, energy system, and transmission, as shown in Fig.2.1. In addition, several connection blocks are also shown in the diagram such as machine control unit, thermal model and drive signal. The machine control strategy is implemented within the machine control block. The thermal model block represents the heat dissipation of electric machine and inverter. The drive signal block provides the reference torque from driver/vehicle. The energy system is represented by a constant DC power supply. This detailed electric powertrain system can be satisfied in different simulation requirements, such as offline, real-time, and hardware-in-the-loop. The following subsections are brief description of each main subsystems.

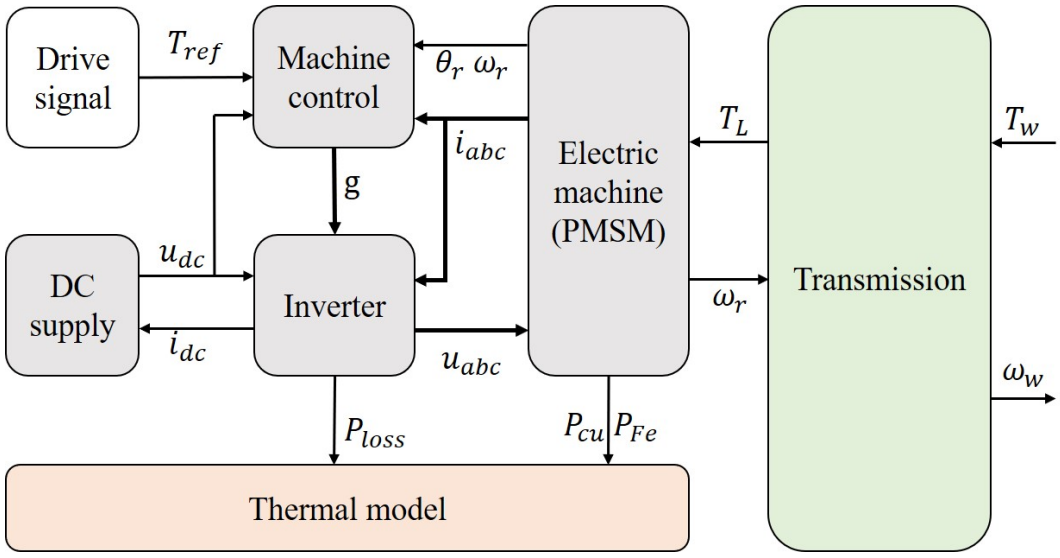

Figure 2.1: Block diagram of the electric powertrain

2.1 Electric Machine

A permanent magnet synchronous machine (PMSM) is considered here. The parameters of the electric machine are given in Table 2.1.

Table 2.1: Parameters of Electric Machine

Parameter	Value	Unit
Rated power	65	kW
Output torque	190	Nm
Rated speed	9000	rpm
Rotation inertia	0.018	kgm^2
Number of pole-pairs	4	-
Stator resistance	0.0267	Ω
No load d-axis flux linkage	0.064	Wb
No-load d-axis inductance	0.46	mH
No-load q-axis inductance	1.3	mH

The electric machine receives the three-phase PWM voltage from the inverter and the load torque from the transmission model. The outputs are the three-phase currents, rotor speed, rotor angle and motor power losses. If the mutual coupling between dq axis is neglected, the derivative of phase currents in d&q frame is described as:

$$L_{di} \cdot \frac{di_d}{dt} = (u_d - R_s \cdot i_d + \omega_m \cdot \psi_q) \tag{2.1}$$

$$L_{qi} \cdot \frac{di_q}{dt} = (u_q - R_s \cdot i_d + \omega_m \cdot \psi_d) \tag{2.2}$$

where u_d, u_q, i_d, i_q are instantaneous d&q axis voltages and currents respectively, ψ_d, ψ_q are flux linkages in d&q axis, R_s represents the stator phase-resistance, L_{di}, L_{qi} are the d&q axis incremental inductances, and ω_m is the mechanical rotor speed. The d&q axis incremental flux linkages can be obtained from the simulation of electric machine FEM model as shown in Fig.2.2. The dotted circle in two subplots is the maximum current of PMSM

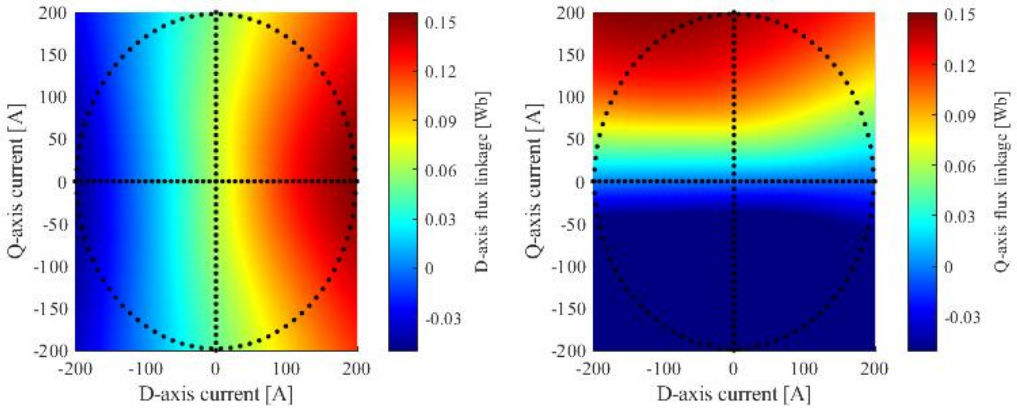

Figure 2.2: d&q axis flux linkage map

The d&q inductances are calculated from the flux linkages based on:

$$L_{di} = \left.\frac{d\psi_d}{di_d}\right|_{i_q=constant} \tag{2.3}$$

$$L_{qi} = \left.\frac{d\psi_q}{di_q}\right|_{i_d=constant} \tag{2.4}$$

Electromagnetic torque can be obtained as:

$$T_e = (\psi_d \cdot i_q - \psi_q \cdot i_d) \cdot p \cdot \frac{3}{2} \tag{2.5}$$

where T_e means the electromagnetic torque, and p is the number of pole-pairs.

However, several electric machine simulation tools are not using the flux linkage as above to calculate currents and voltages. Only d&q axis inductances are involved as shown in the following equations:

$$L_{da} \cdot \frac{di_d}{dt} = v_d - R_s \cdot i_d + L_{qa} \cdot \omega_e \cdot i_q \tag{2.6}$$

$$L_{qa} \cdot \frac{di_q}{dt} = v_q - R_s \cdot i_q + L_{da} \cdot \omega_e \cdot i_d - \psi_P \cdot \omega_e \tag{2.7}$$

$$T_e = \frac{3}{2} \cdot p \cdot [\psi_P \cdot i_q + (L_{da} - L_{qa}) \cdot i_d \cdot i_q] \tag{2.8}$$

where u_d, u_q , i_d, i_q are instantaneous d&q axis voltages and currents; R_s is stator phase resistance; ψ_P is the magnet flux linkage, and ω_e is the electrical rotor speed. In this case,L_{da} and L_{qa} are apparent inductances in d&q axis in addition to the incremental inductances in equation 2.1 and 2.2. Apparent inductance is the interpolation based on incremental flux linkages $\psi_d i \& \psi_q i$ and the corresponding d&q currents shown as follow:

$$L_{da} = \frac{\psi_d - \psi_{d0}}{i_d} \tag{2.9}$$

$$L_{qa} = \frac{\psi_q - \psi_{q0}}{i_q} \tag{2.10}$$

where ψ_{d0} and ψ_{q0} are the flux linkages at zero current point. Fig.2.3 and Fig.2.4 shows the difference between apparent and incremental inductance in 2-D and 3-D plot, respectively.

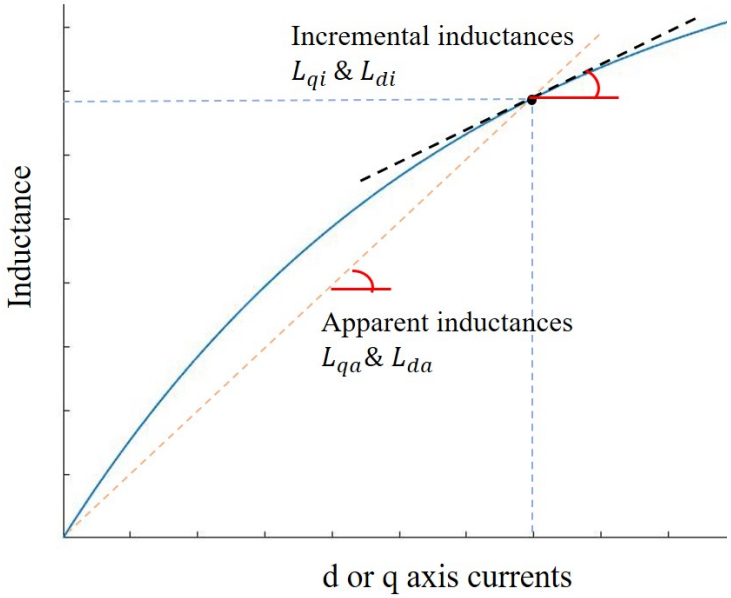

Figure 2.3: The meaning of apparent and incremental inductance in 2-D plot

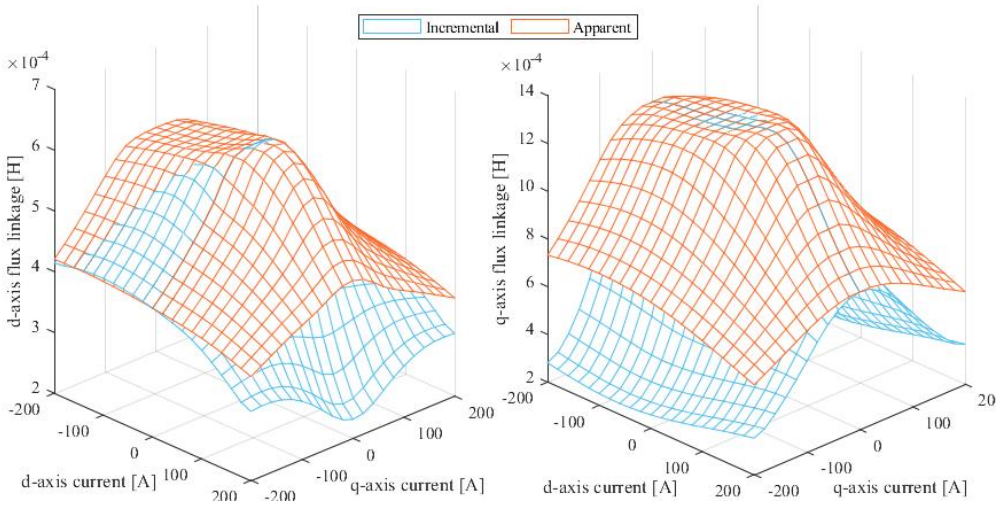

Figure 2.4: The comparison of apparent and incremental inductance in 3-D plot

Two different descriptions of PMSM will lead to different torque performance, and this will be discussed in the results section. In this thesis, all testing cases are using the flux linkage PMSM to simulated electric powertrain, i.e., equation 2.1, 2.2, and 2.5.

The rotor speed in two simulation methods are same, which is calculated by the following equation:

$$J \cdot \frac{d\omega_r}{dt} + B \cdot \omega_r = T_e - T_L \tag{2.11}$$

where T_L is load torque, ω_r is rotor speed, J is rotating inertia and B is viscous damping constant. The mechanical friction losses are neglected in this case. Therefore, B is assumed to be zero. Rotor angle can be calculated by the integration of the rotor speed. Since the electric machine is connected to the gear box and wheels via shafts, the inertia J indicates the combined inertia as follow

$$J = J_m + J_g^{'} + J_w^{'} \tag{2.12}$$

where J_m indicates the inertia of electric machine, $J_g^{'}$ and $J_w^{'}$ are inertia of the gearbox and wheel observed from the electric machine side, respectively.

2.2 DC supply and Inverter

The circuit diagram of DC battery supply and inverter is shown in shown in Fig.2.5. The battery model is a constant voltage source combined with internal resistance, capacitance, and inductance. The inverter is modeled as a six-MOSFETs (Q1 to Q6) 2-level voltage source converter (VSC). The battery and inverter are connected by DC cable along with capacitor and resistor. In vehicle model, power electronics are modelled as loss components with a simple input and output power relationship. Table 2.2 presents all parameters of DC supply and inverter in powertrain model.

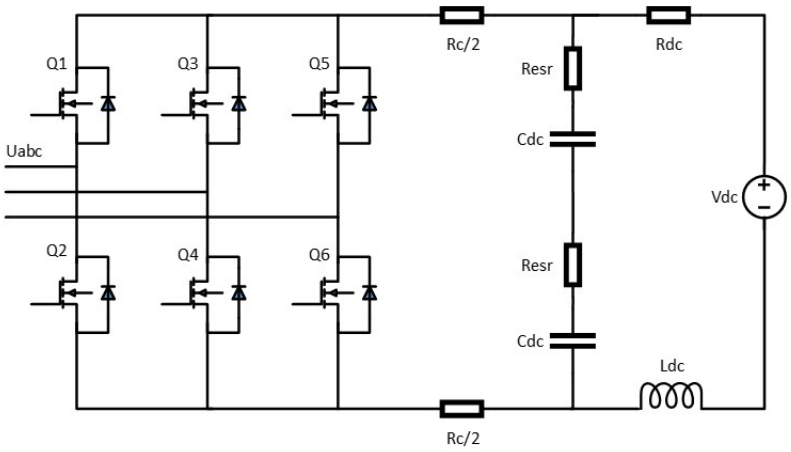

Figure 2.5: The circuit diagram of DC supply and inverter in powertrain

Table 2.2: Parameters of DC Supply and Inverter

Name	Symbol	Value	Unit
DC link voltage	U_{dc}	360	V
resistance of DC battery	R_{dc}	1	mΩ
Inductance of DC battery	L_{dc}	0.5	mH
ESR of DC link capacitor	R_{esr}	0.865	mΩ
DC link capacitance	C_{dc}	150	μF
DC cable resistance	R_c	1	mΩ
Switching frequency of inverter	f	16	kHz

The losses in power electronics are summarised into switching and conduction losses [25]. Switching losses consist of the turn-on and turn-off losses in MOSFETs and diodes. Conduction losses contains DC cable losses in addition to MOSFETs and diodes losses. All these values are calculated based on current, voltage, and frequency. The power relationship of DC supply and inverter are shown as follow:

$$P_{Battery} = P_{dc} - P_{loss/dc} \tag{2.13}$$

$$P_{loss/INV} = 6 \cdot \left[P_{F,T/INV} + P_{D,T/INV} + \sum_{i=1}^{3} (P_{SW/INV})_i \right] \tag{2.14}$$

where $P_{Battery}$ and P_{dc} are battery power and DC link power, $P_{SW/INV})_i$ are three switching loss components, and $P_{F,T/INV}$ and $P_{D,T/INV}$ are conduction losses of a MOSFET and diode in inverter respectively.
In this work, the inverter receives gate signals from the machine control block where a field-oriented control (FOC) is implemented [26].

2.3 Machine Control

In machine control, a cascaded control strategy is shown in Fig.2.6 and 2.7. Both the outer loop speed controller and inner loop current controller are used based on the field oriented control (FOC) strategy.

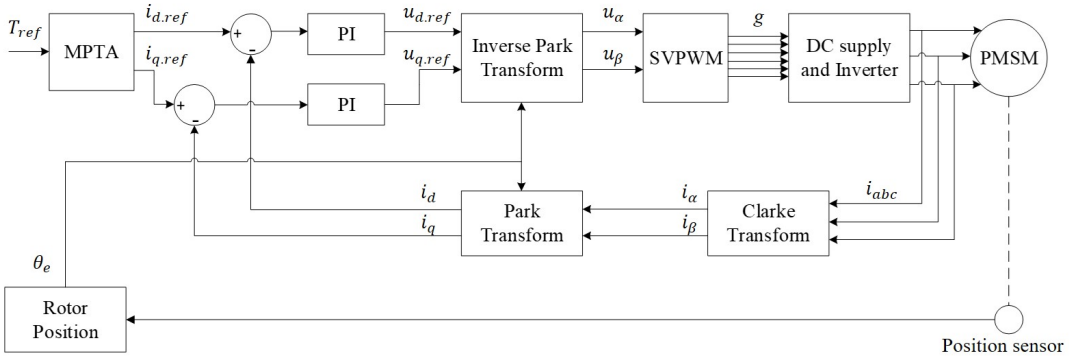

Figure 2.6: Block diagram of current controller layer in PMSM

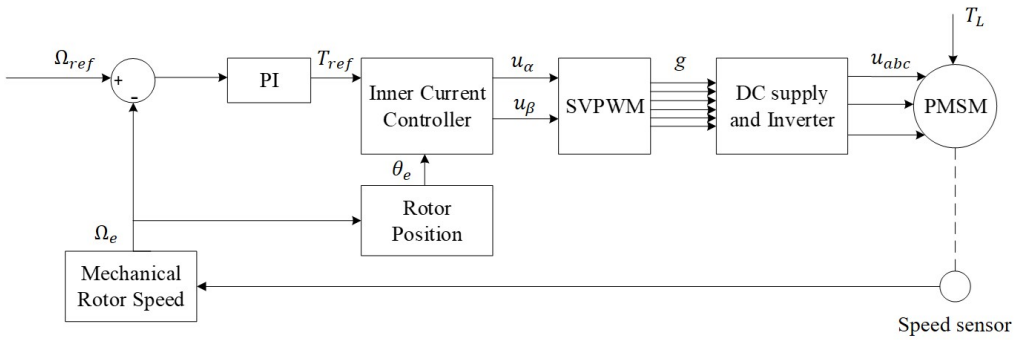

Figure 2.7: block diagram of speed controller layer in PMSM

In electric machine control [26], stator currents i_{abc} are measured using electric current sensor. The d&q axis currents are calculated from three phase currents via Clarke and the Park transform. Then it can be used as the feedback values of the current control loop. The reference torque is transformed to d&q axis reference currents based on maximum torque per ampere (MPTA) method [27]. The deviations between reference and measured d&q currents go through the electric current PI controller, and the respectively output phase voltages $u_{d.ref}$ and $u_{q.ref}$ on the d&q axis system. $u_{d.ref}$ and $u_{q.ref}$ are transformed into the stator phase voltage u_α and u_β under $\alpha\&\beta$ coordinate system via inverse Park transform. Then, using the voltage space vector PWM method to produce PWM gate signals g to control the inverter, thus enabling closed-loop control of the PMSM. The PI control parameters are calculated based on following equations:

$$u(t) = K_p e(t) + K_i \int e(t)dt \tag{2.15}$$

$$R_a = \alpha_c L(J) - R(B) \tag{2.16}$$

$$k_p = \alpha_c L(J) \tag{2.17}$$

$$k_i = \alpha_c \left(R(B) + R_a\right) \tag{2.18}$$

where $e(t)$ is the error between reference and actual value in current and speed, $u(t)$ is the output of PI controller, α_c is the current and speed controller bandwidth, and k_i, k_p, and R_a are integral, proportional, and active damping parameters respectively. In current controller, L and R are d&q inductance and stator resistance. In speed controller, L and R are replaced by J (motor inertia) and B (viscous damping) accordingly.

In this case, the i_d=0($i_{d.ref}$ =0) torque transform method can also be used for currents reference calculation. The parameters of machine controller are shown in Table 2.3 and these values are calculated based on no-load parameters of PMSM in Table 2.1.

Table 2.3: Parameters of Machine Controller

Parameter	**Value**
Bandwidth of current controller	1500
Bandwidth of speed controller	150
Proportional gain of current controller d-axis	0.6843
Proportional gain of current controller q-axis	1.881
Proportional gain of speed controller	1.316
Active damping constant d-axis	0.6576
Active damping constant q-axis	1.8543
Active damping constant speed controller	0.175
Integral gain of current controller d-axis	1026
Integral gain of current controller q-axis	2821
Integral gain of speed controller	197.43

2.4 Transmission

The transmission is modelled with an ideal gearbox connected to electric machine and wheel, as shown in Fig.2.8. Both sides of torque and inertia can be converted to each other according to the transmission ratio.

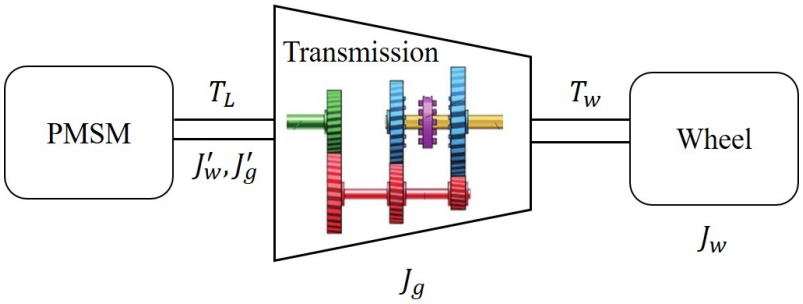

Figure 2.8: Transmission system between electric machine and wheel

The efficiency of the gearbox is grouped into torque losses. The gearbox contains multiple reduction stages, which rotate at different speeds. The inertia of the gearbox is therefore calculated by translating the inertia of each gear into the electric machine shaft. The inertia of a gearbox with n gear stages can be defined as

$$J_g^{'} = J_1 + \frac{(J_2 + J_3)}{k_1^2} + \cdots \frac{(J_{n-2} + J_{n-1})}{k_1^2 \cdot k_2^2 \cdots k_{n-1}^2} + \frac{J_n}{k_g^2} \tag{2.19}$$

where J_1 to J_n represents the inertia of each gear wheel, the suffix J_1 indicates the gear wheel that rotates at the rotor speed of the motor and J_n is the final gear wheel which rotates at the same speed as wheel. The co-efficient k_1 to k_{n-1} is the reduction ratio for each stage, with k_1 being the first stage, closest to the electric motor shaft. Finally, k_g means the final gear ratio.
The inertia of each wheel in 2.12 is calculated like gearbox as below:

$$J_w^{'} = \frac{J_w}{k_g^2} \tag{2.20}$$

The load torque in 2.11 is obtained as:

$$T_L = \frac{T_w}{k_g} - T_{loss} \tag{2.21}$$

where T_{loss} is the gearbox torque losses and T_w is load torque at wheels. The wheel speed Ω_w is calculated by scaling down the electric rotor speed by the gear ratio k_g. In this work, the transformed gear ratio is 14.

2.5 Thermal Modeling

Simplified lumped-parameter thermal networks (LPTNs) are used to model the heat dissipation of electric machine and inverter as shown in Fig.2.9 and Fig.2.10. The

LPTN for electric machine in Fig.2.9 contains seven internal nodes representing the rotor core, permanent magnets, air gap, stator tooth, stator yoke, stator frame and coolant. The LPTN for the inverter in Fig.2.10 contains three nodes representing the case, heat-sink and ambient.

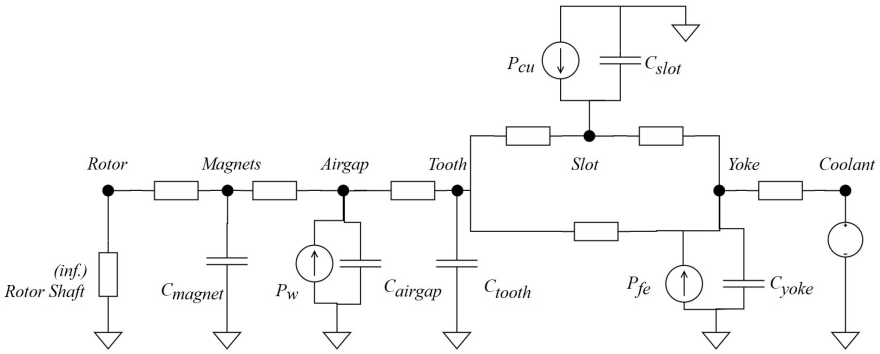

Figure 2.9: Seven nodes LPTN of PMSM

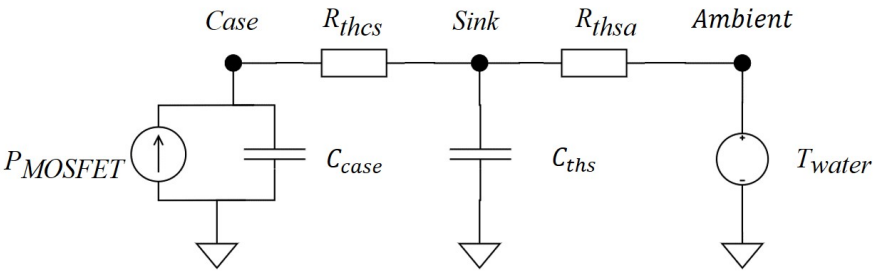

Figure 2.10: Three nodes LPTN of inverter

In electric machine, the seven node thermal circuit is modeled based on the hairpin four-layer winding PMSM as shown in Fig.2.11.

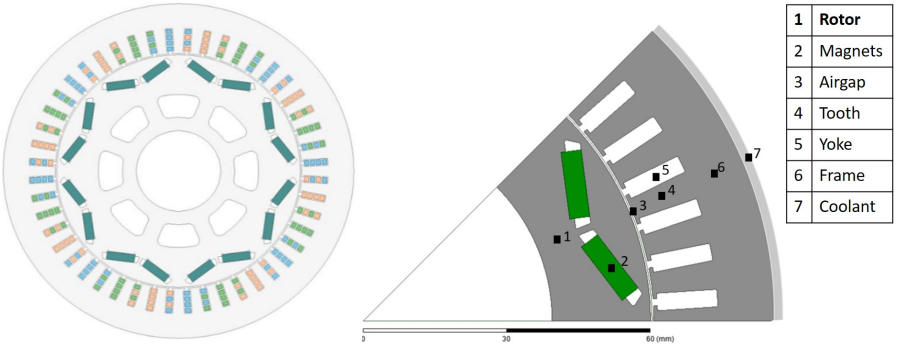

Figure 2.11: Seven nodes diagram of hairpin winding PMSM

The rotor core node is connected with the permanent magnets by thermal conduction. This lumped part makes heat transfer through rotor regions, then the heat convection passes through the air gap with windage or friction losses. The thermal resistance connects the stator winding, the insulation, and the stator core. In this thermal model, it is assumed that the main heat flow is generated from stator winding and stator iron core, i.e., the copper and iron losses[27]. The total heat losses are dissipated finally in the coolant. This way the node of coolant is simplified as a fixed value.

The copper losses are calculated as below:

$$P_{cu} = \frac{3}{2} \cdot \left(i_d^2 + i_q^2\right) \cdot R_s = \frac{3}{2} \cdot i_s^2 \cdot R_s \tag{2.22}$$

The iron-core losses at the frequency f are calculated as follow:

$$P_{fe}\left(i_d, i_q, f\right) = \frac{f \cdot \left(k_h + f \cdot k_c\right)}{f_{\text{base}} \cdot \left(k_h + f_{\text{base}} \cdot k_c\right)} \cdot P_{fe}\left(i_d, i_q\right) \tag{2.23}$$

where k_h,k_c are coefficients of hysteresis losses and classical eddy current losses. At the base speed represented by f_{base}, the iron-core loss map P_{fe} as a function of i_d and i_q can be calculated in the FEM model.

In thermal modeling, the mode of heat transfer consists of conduction, convection, and insulation. In general, most parts of the machine components like magnets, iron, and copper materials are simulated with conduction mode [28]. The formulas of heat conduction resistance in radial and tangential directions are described as follow, and shown in Fig.2.12.

$$R_{\text{radial}} = \frac{\ln\left(r_0/r_i\right)}{2\pi \cdot l \cdot \lambda} \tag{2.24}$$

$$R_{\text{tangential}} = \frac{l}{s \cdot \lambda} \tag{2.25}$$

where r_i and r_0 indicate inner and outer radius of annulus, l is the length of the part in the heat flow direction, s is the cross-sectional area, and λ is the thermal conductivity.

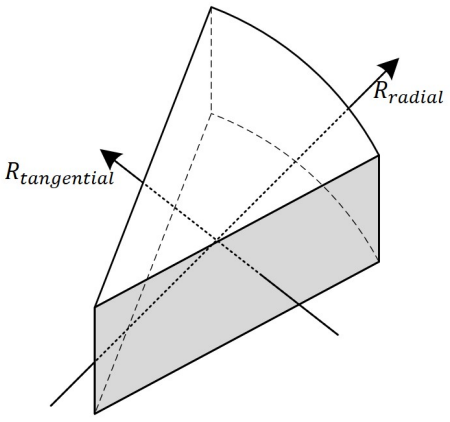

Figure 2.12: Pie-section of a cylinder showing radial and tangential direction

The physical parameters of PMSM are listed in Table 2.4 and the thermal conduction coefficients of each region are shown in Table 2.5.

Table 2.4: Physical Parameters of PMSM

Parameter	**Value**	**Unit**
Length of Airgam	0.7	mm
Length of Stacking	120.0	mm
Outer Diameter of Stator	175.0	mm
Inter Diameter of Stator	123.0	mm
Outer Diameter of Rotor	121.6	mm
Inter Diameter of Rotor	42.0	mm
Width of Slot	14.2	mm
Slot Thickness of Slot	4.3	mm
Width of PM	14.0	mm
Thickness of PM	4.1	mm

Table 2.5: Material Parameters of PMSM

Material	**Conductivity** λ $W/m/k$	**Density** ρ g/cm^3	**Heat Capacity** C_ρ $J/g/K$
Copper	384	8.93	0.385
Steel	50	7.9	0.466
Insulator	0.5	1.2	1.1
Permanent Magnet	8	7.5	0.45
Air (40)	0.28	0.001	1

The thermal capacitance, for transient analysis, can be calculated as below:

$$C = \rho \cdot V \cdot C_\rho \tag{2.26}$$

where ρ is density, V is volume of each part, and C_ρ is the heat capacity of each material. The parameters of each component are shown in Table 2.5.

The heat dissipation of airgap in convection mode can be modeled using a thermal resistance.

$$R_{\text{conv}} = \frac{1}{A\lambda} \tag{2.27}$$

where λ is the air thermal conductivity, and A is a cylinder area whose radius is equal to airgap intermediate radius as shown by right in Fig.2.13.

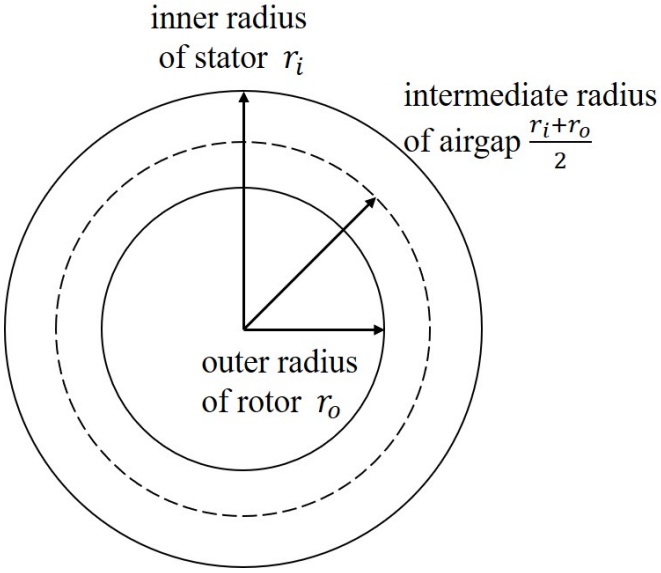

Figure 2.13: 2D cross-section of a cylindrical electric machine

In inverter thermal circuit Fig.2.10, each node connects each other by thermal resistance and capacitance. The thermal circuit shows the heat transfer from converter case to cooling plate and sink, then flows to the ambient. The ambient node is where the temperature eventually dissipates to outside, so it is set to a fixed value.

In this case, the heat source is the combination of six-MOSFETs power losses, i.e., the switching losses and the conduction losses as shown in equation2.14. The calculation of each thermal node is same as PMSM, so this part is simplified to final parameters as shown in Table 2.6.

Table 2.6: Thermal Parameters of Inverter

Parameter	**Value**	**Unit**
Thermal Resistance Sink-Ambient	0.0073	K/W
Thermal Resistance Case-Sink	0.0043	K/W
Thermal Capacitance of Sink	1238	J/K

3

Vehicle Modeling

The schematic of vehicle model in CarMaker platform, including models of driver, vehicle controller, autobody & wheels, road & environment, and electric powertrain is shown in Fig.3.1. A rear-wheel-drive (RWD) vehicle with parameters shown in Table IV is considered in this work. The motion of the vehicle is modeled in three dimensions: longitudinal, lateral and vertical. In addition, different driver behaviour in terms of acceleration can be simulated. Road traction/braking limits determined by tyre adhesion can also be included. In the following subsections, these models are described. In addition, a wheel slip control unit is also introduce in this section, and it build inside the steer & brake system. Since, the wheel slip control block is not the main purpose of this paper, it is not shown in the block diagram of vehicle modeling.

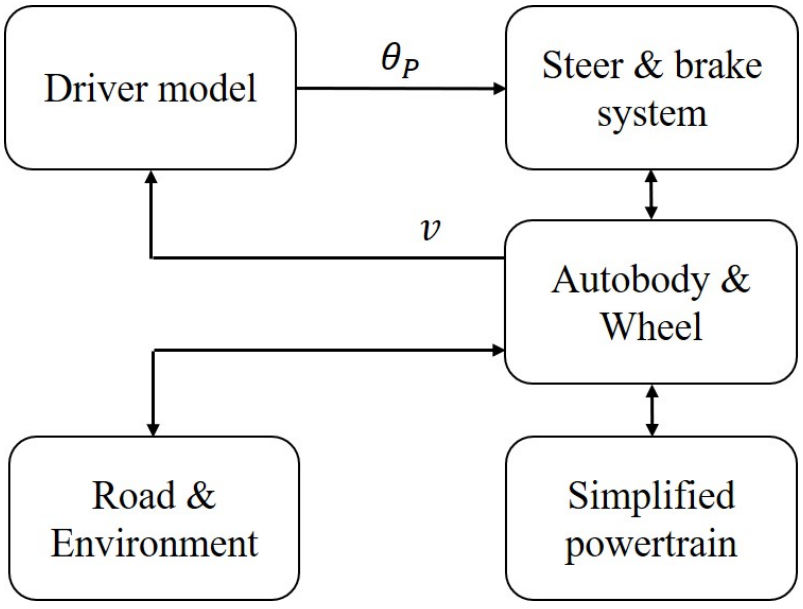

Figure 3.1: block diagram of vehicle modeling

Table 3.1: Parameters of Vehicle Model

Parameter	Value	Unit
Unladen mass	1745	kg
Wheel inertia	2.673	kg/m^2
Wheel radius	0.343	m
Cross-sectional area of the vehicle	2.168	m^2
Aero-dynamic drag co-efficient	0.3	-
Rolling resistance co-efficient	0.009	-
Gear ratio	7	-
Number of drive units	2	-
Acceleration due to gravity	9.8	m/s^2

3.1 Autobody and wheel

The simulated vehicle is a multi body system including vehicle body, vehicle loads, wheels, suspensions, and aerodynamics[]. The vehicle center of gravity (COG) is considered for calculating the force on each wheel. Therefore, the load transfer between the front and rear axles can be modeled, which affects the maximum traction force on each wheel. In addition, the aerodynamic force is modeled as a sum of drag, side and lift forces. Similarly, the rolling resistance force considers of roll, pitch and yaw movement of the vehicle.

To obtain the typical behavior of vehicle during wheel slip control study. Only the longitudinal motion of vehicle is considered. The tire-road resistive force F_r consists of aerodynamic force F_{aero}, gradient force F_{grad}, and rolling resistance F_{roll}, as shown below:

$$F_r = F_{aero} + F_{grad} + F_{roll} \tag{3.1}$$

$$F_{aero} = \frac{1}{2}\rho \cdot C_d \cdot A \cdot v^2 \tag{3.2}$$

$$F_{grad} = m \cdot g \cdot sin\alpha \tag{3.3}$$

$$F_{roll} = C_r \cdot m \cdot g \tag{3.4}$$

where r_w is radius of wheel, n_d is the number of drive units, in this work, n_d equals to 2, ρ is air density, C_d is aerodynamic drag co-efficient, A indicates effective cross-section area, C_r presents the rolling resistance co-efficient, g is gravity acceleration and α is gradient angle of road. The relation between torque and force is shown as follow:

$$T = r_w \cdot F \tag{3.5}$$

Then the resistance torque on each driven wheel can be calculated as

$$T_r = \left(\frac{1}{2}\rho \cdot C_d \cdot A \cdot v^2 + C_r \cdot m \cdot g + m \cdot gsin\alpha\right) \cdot \frac{r_w}{n_v} \tag{3.6}$$

where n_v is the number of wheels on vehicle (normally it equals to 4). Based on the electric machine equation 2.11, 2.12 and 2.21, the rotational speed of each rear-drive wheel can be calculated as:

$$\frac{J}{k_g} \cdot \frac{d\omega_w}{dt} = T_w - T_r \tag{3.7}$$

where T_w is the driving torque transformed from electric machine T_e to gearbox. The equation is simplified without slip ratio, braking torque, and torque loss in gearbox. The following equation shows the rotational speed of front non-drive wheels

$$J_w \cdot \frac{d\omega_w}{dt} = T_r \tag{3.8}$$

where T_w and k_g are equals to zero due to no-connection with electric machine, and J_w is only the wheel inertia instead of electric machine and gearbox. The positive resistive torque of front wheel is show the opposite direction compare to the rear-drive wheel. The relationship between vehicle and wheel speed can be formulated as follow:

$$\lambda = \frac{r_w \cdot \omega_w - v}{r_w \cdot \omega_w} \tag{3.9}$$

where λ is the wheel slip ratio. $\lambda \to 1$ indicates increasing slip, and $\lambda \to 0$ represents decreasing slip.

Based on newton's second law, the longitudinal vehicle acceleration can be derived as:

$$m \cdot \dot{v} \quad = n_d \cdot F_w - n_v \cdot F_r \tag{3.10}$$

where F_w and F_r are load force and resistance force of each wheel accordingly, n_d is the number of driven wheels ($n_d = 2$ in this case).

3.2 Driver Modeling

The driver model or driving maneuver consists of driving missions and driver behaviors. The driving missions can be grouped into speed-based and distance based driving cycles, and the driver behaviors are considered: aggressive, normal, and defensive as shown in Fig.3.2 . The x and y axis indicate lateral and longitudinal motions respectively, while the positive and negative values on each axis represent acceleration and deceleration, accordingly.

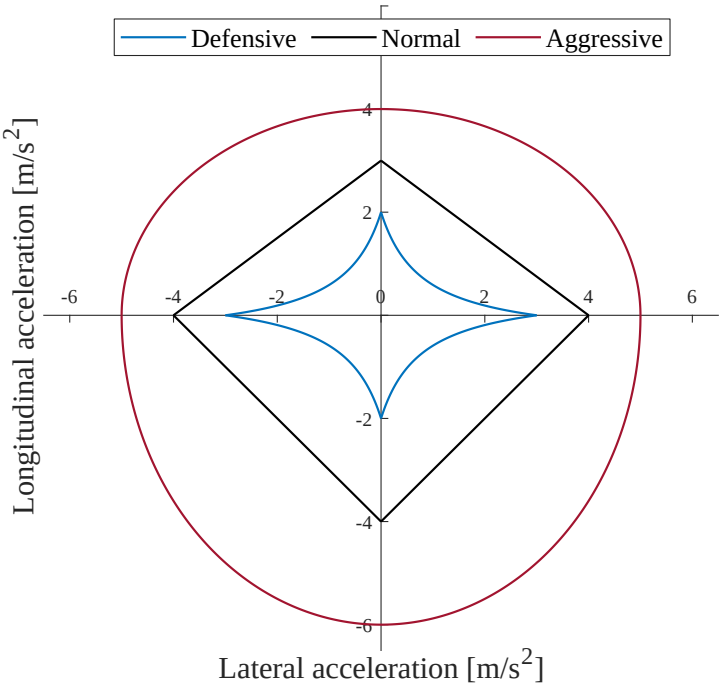

Figure 3.2: Three typical driver models

For the aggressive driver the maximum deceleration can be much higher compared to the acceleration, and both vary considerably. Defensive drivers result in a narrow range of acceleration and deceleration, and they have the same maximum value. The normal driver represents a driving behaviour in between the two mentioned above. Other driving models can be adapted as required. The output of the driver model is the pedal position angle θ_p. The driving torque is obtained by multiplying the pedal position and the speed-based maximum torque of the electric electric powertrain.

3.3 Steer and brake system

The main idea of the Steer and brake system is to separate the connection between driver model and autobody wheel model. the driver module provides the required values for pedal position, brake, clutch, steering angle, etc. The Steer and brake system decides, on request, in which way the required signals from driver are to be converted to the vehicle modules (powertrain, brakes, steering, etc.).

Fig.3.3 plots the relationship between vehicle speed and maximum output torque based on PMSM. The maximum torque at each speed multiplied by pedal position θ_p is the reference torque supplied to the electric powertrain, e.g., T_{ref}.

For example, When the motors are operating at 4000 rpm, the maximum output torque of each motor at this time is 104 Nm. If the driver presses the gas pedal to the floor ($\theta_p = 1$), the total output torque (two driving motors) at this point is 104*1*2=208 Nm.

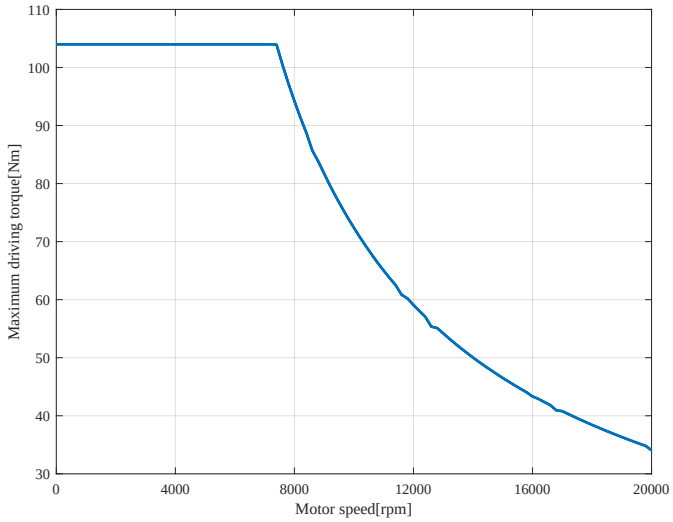

Figure 3.3: Relationship between maximum output torque and speed

In addition, the braking system in Fig.3.4 is integrated in load torque T_w and electric driving torque T_e. The role of the brake system is to calculate the current braking torque for each wheel (wheel and parking brake). The brake control communicates the target regenerative braking torque for each wheel to powertrain based on the maximum possible regenerative braking torque of the motor and the redistribution strategy. And the brake system sends the mechanical brake torque to each wheel. In combination with the ECU, it is possible to set a target drive source torque for the powertrain control. In the vehicle modeling, all braking torques are transmitted as negative values.

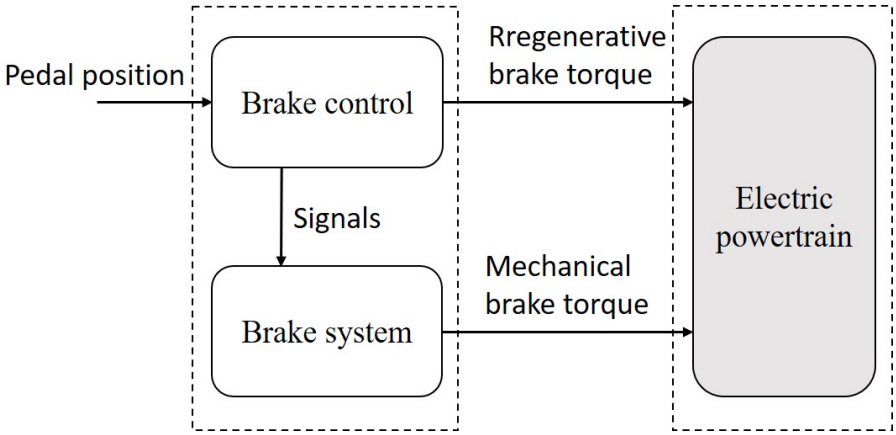

Figure 3.4: block diagram of braking system

3.4 Road and Environment Modeling

The road and environment models describe tire-road contact, traffic conditions, and vehicle trajectories. The maximum traction force transferred to wheels is expressed as:

$$F_{w,max} = \mu \cdot F_N \tag{3.11}$$

$$F_N = \frac{m \cdot g \cdot cos\alpha}{n_v} \tag{3.12}$$

where μ is friction coefficient, F_N is normal force acting on each wheel, n_v is the number of wheels on vehicle i.e., $n_v = 4$, and other values are same as 3.1. The friction coefficient varies with different road and slip ratio, since it is not important in the thesis, the description is removed.

When the traction force applied to the wheel exceeds the value given in 3.11, the wheel will start to slip, i.e., the slip ratio λ in 3.9 starts increasing. The road gradient and environment conditions, e.g. temperature, air density, air pressure, etc., are also available for modeling. Fig.3.5 and 3.6 show two types of road and environment models in thermal model test case and wheel slip control test case, respectively.

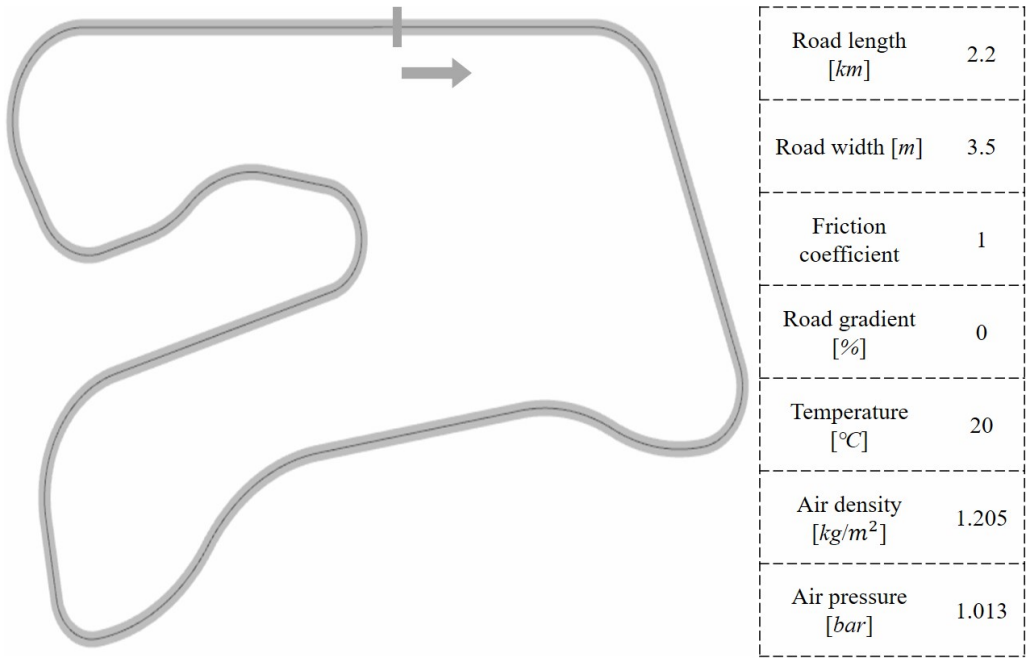

Figure 3.5: Road and environment model 1

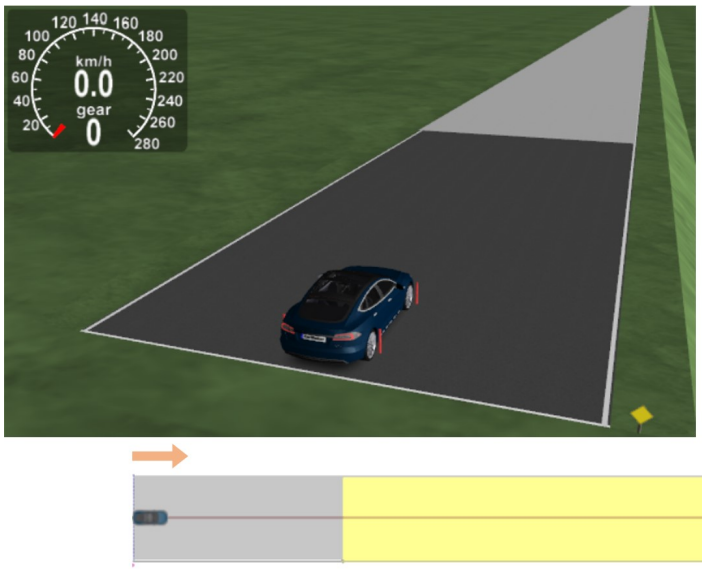

Road length [m]	100
Road width [m]	10
Friction coefficient	1 (dark) 0.2 (yellow)
Road gradient [%]	0
Temperature [°C]	20
Air density [kg/m^2]	1.205
Air pressure [bar]	1.013

Figure 3.6: Road and environment model 2

3.5 Simplified electric powertrain Modeling

The electric powertrain which acts as a power system inside CarMaker is divided into a number of subsystems with well defined interfaces, as shown in Fig.3.7. The powertrain is assigned to three levels: powertrain control unit, subcomponent control units(BCU, MCU, TCU) and electro-mechanic components. Powertrain control unit contains a top-level powertrain control strategy that mainly manages the working states (e.g. ignition on, drive) and the distribution of electrical and mechanic energy.

In second-layer, three control units are involved, the battery control unit(BCU), the motor control unit (MCU), and the transmission control unit (TCU)). Each control unit supervises one kind of electro-mechanic components in order to establish the energy distribution planned by powertrain control unit.

The subsystems of the third level are models of the powertrain's electro-mechanic components (such as motors, gearboxes, batteries etc.). However, all of these electro-mechanic components are described ideally with basic equations, such as only using equation2.11 to describe the electric machine. Therefore, the detailed dynamics of electric machine like currents, voltages, and frequency are unavailable in this platform.

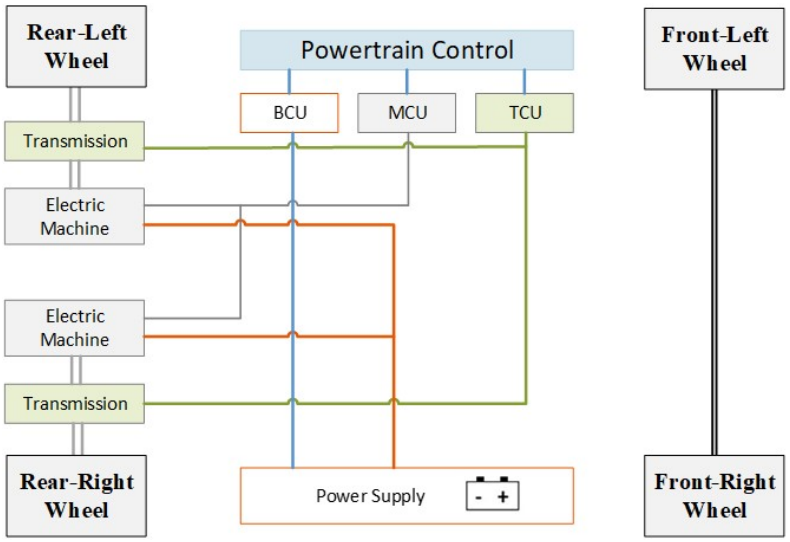

Figure 3.7: Three-level simplified powertrain model in RWD vehicle

3.6 Wheel slip control

For traction and stability control, different models that represent the tire-road interaction have been used. In this thesis, the aerodynamic-free acceleration vehicle model with the magic formula is used owing to its semi-empirical, simple, and low-cost computation properties. The wheel slip control is based on the 'bicycle' model that only considers the rotation rear wheel dynamic and the longitudinal movement. And the vehicle traction is performed by two independently controlled in-wheel electric motors, placed on each rear wheel. Electric motors are driven by variable speed drives able to apply the reference torque in the order of milliseconds, which allows neglecting the dynamics of the actuators.

3.6.1 Vehicle motion analysis

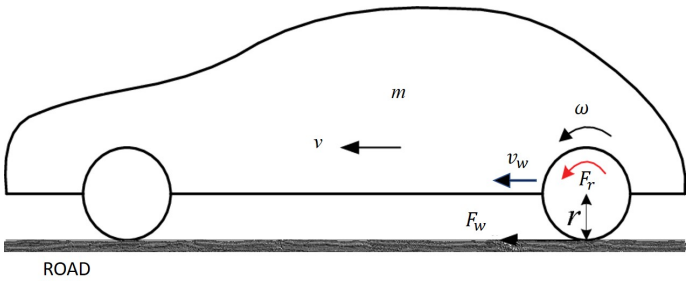

Figure 3.8: Longitudinal vehicle dynamics

Fig.3.8 shows the longitudinal vehicle dynamics, when only the longitudinal vehicle motion is considered, the dynamic differential equation for the in-wheeled motor can

be described as follow

$$J \cdot \dot{\omega} \quad = T_e - \frac{r \cdot \mu \cdot m \cdot g}{4} \tag{3.13}$$

this equation is the combination of 2.11, 2.12, 3.5, 3.11 and 3.12.

And all the vehicle dynamics in 3.9, 3.10, 3.5, and 3.11 are summarized as follows:

$$m \cdot \dot{v} \quad = F_w - F_r \tag{3.14}$$

$$v_w = r \cdot \omega \tag{3.15}$$

$$F_w = F_{w,max} = \mu \cdot F_N \tag{3.16}$$

$$\lambda = \frac{v_w - v}{v_w} \tag{3.17}$$

where v and v_w are vehicle and wheel linear speeds, respectively. Other values are same as above.

The main idea of proposed wheel slip control is improving the vehicle behavior under extreme conditions like ice-road. During the acceleration period, the vehicle stability and motor efficiency are more important than purely apply the absolute maximum driving force to the vehicle. To reduce the unnecessary slip energy loss, we can apply a well-managed control of the wheel acceleration and speed when vehicle drives into the low friction road. If the acceleration of each wheel difference can be controlled, then the slip-ratio is also well-controlled.

For normal road, the acceleration of each wheel is limited by the maximum driving torque and the resistance force. These values will converge to constant since there is no slip, i.e., the derivative of slip ratio λ in 3.17 will equal to zero during stable acceleration phase.

When vehicle drives into the ice-road, low tire-road friction coefficient μ, the wheel velocity will be increased abnormally owing to the extreme low friction forces in equation 3.16. The acceleration $\dot{\omega}$ or a of the slipped wheel jumps as well, which means the derivative of wheel acceleration $\dot{a}$ will over some normal condition. Therefore, this value can be treated as a threshold to trigger the novel acceleration-based load torque compensation wheel slip control.

3.6.2 Control Method

At the beginning, the previous no-slip wheel acceleration value is settled as the reference value ω_0 . The first step is reducing the reference driving torque T_e or T_{ref} according to the decreasing resistance torque to keep the wheel acceleration as

reference ω_0.

At the meantime, the total losses of load torque during slip can be accumulated by

$$\Delta T_d = \sum_{t0}^{t1} (\dot{\omega} - \dot{\omega}_0) \cdot J \tag{3.18}$$

where t_0 and t_1 means the starting and ending time of first step wheel slip control, respectively.

According to equation 3.14, the acceleration of vehicle/chassis v will be influenced by the lost load torque ΔT_d, shown as follow

$$\Delta \dot{V} = \frac{2\Delta T_d}{rm} \tag{3.19}$$

This value means that the acceleration value of vehicle and wheel are not close to each other, i.e., $\dot{V} \neq r\dot{\omega}$. The slip ratio λ will still rise according to equation 3.17. Therefore, the vehicle still needs extra control to remain stable.

The second step control is to regulate the acceleration of the chassis to its previous no slip state. So, the extra torque created in equation 3.19 should be reduced. As mentioned above, the first step happens quickly, and the slip ratio is still close to zero. Then, we can get the second step reference torque compensation equation as

$$\Delta T_{\text{ref .2}} = \frac{2\Delta T_d}{r^2 m} \cdot J \tag{3.20}$$

Until now, the acceleration of chassis and wheel are maintained at no slip situations, thereby the vehicle can remains stable.

The block diagram of proposed controller is shown in Fig.3.9.

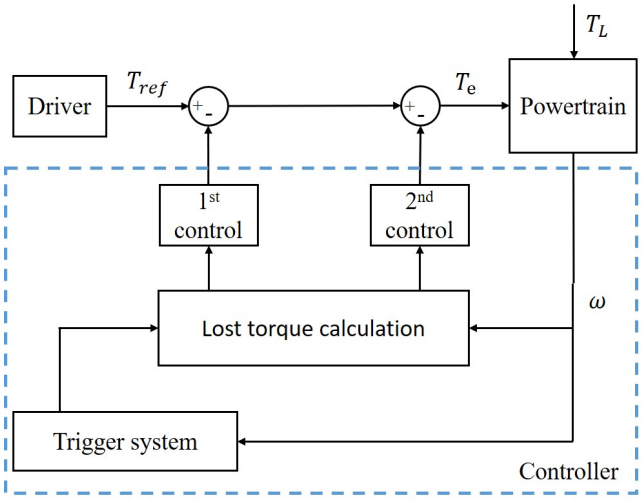

Figure 3.9: The block diagram of proposed controller

With this controller, the traction force can be limited to its maximum effective values owing to road adherence. And it does not restrict the vehicle traction torque on normal roads (not triggered yet). Compare to other controllers mentioned in reference, this controller only need wheel or motor speed as input signal, so the control complexity can be reduced.

On the other side, this approach also can be used for Anti-lock Braking System (ABS). The conventional hydraulic braking system can be replaced by the regenerative brake with rechargeable batteries. The main idea is to regulate the wheel and vehicle slip ratio to their previous no-slip states when its braking. While this strategy should combine with slip ratio estimation which will not be discussed in this paper. Only a simplified case study is proposed in simulation based on the proposed control strategy.

4

Model Coupling Method

The detailed electric powertrain and vehicle model needs to be interfaced to create the high-fidelity full-vehicle system. The vehicle has two electric drive systems driveing the two rear wheels independently, as shown in Fig.3.7. At the very first stage, the simulation time steps used by both models to advance the time evolution of the system dynamics should be the same in order to keep them synchronized. In this thesis, all the simulation time steps are defined as 1 millisecond. Four different coupling methods are discussed in the following sections.

4.1 Torque open-loop coupling method

Fig.4.1 describes the signal interfaces of torque open-loop method between vehicle model (CarMaker) and electric powertrain system. All input signals from vehicle model to electric powertrain are the driving torques T_{ref} and the wheel load torques T_w, and the outputs of electric powertrain are motor/wheel speeds. In this method, vehicle model and external electric powertrain are operating in parallel, there are no signals feedback to vehicle. Therefore, the external electric powertrain does not influence the vehicle simulation.

Vehicle model (left parts) receives the driving signal as discussed before. The driving torque T_{ref} and load torque T_w signals are obtained from the driver and autobody, respectively. Then, each motor/wheel speed ω_w can be calculated by the simplified electric powertrain in vehicle model based on equation2.11, and feedback to vehicle body to finish the simulation.

The external electric powertrain (right parts) receives two torque signals from vehicle and calculates the morot/wheel speed at the same time. In this method, the electric machine is using the current/torque control in addition to the speed control as shown in Fig.2.6. As long as both motors/wheels rotate at the same speed, the external electric powertrain simulation can be used. This coupling method is only used to test the electric machines, inverter and control functionalities. The powertrain model in this case acts as an observer for vehicle simulation. Therefore, providing access to measure power, voltage, currents, efficiency, etc.

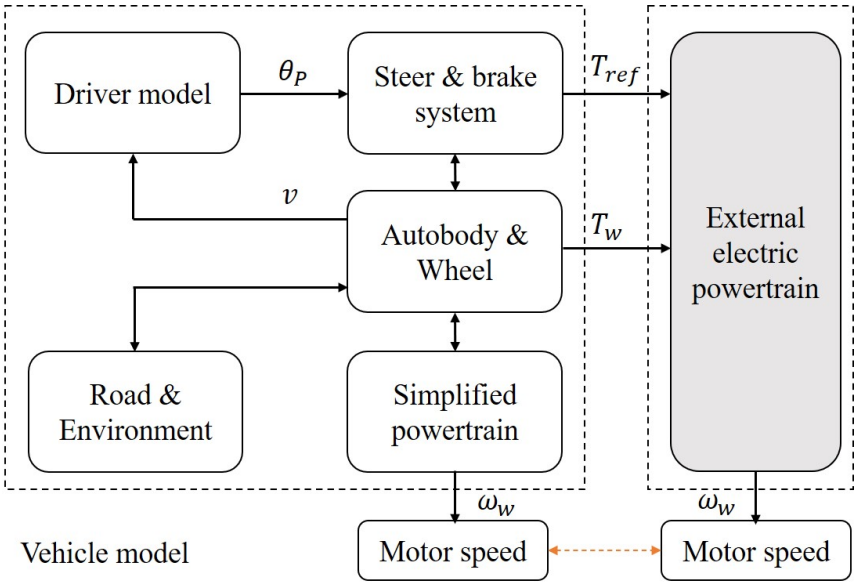

Figure 4.1: Torque open-loop coupling method between vehicle and electric powertrain

4.2 Torque close-loop coupling method

In the torque closed-loop interface, as shown in Fig.4.2, the speed signals of each rear wheel are feedback to the vehicle simulation. The front wheels models are still using the simplified powertrain in vehicle model, because only two electric drive needs to be simulated. The external powertrain is acting as the main power system in vehicle simulation instead of an observer. However, this interface is less demanding on real machine test bench, because the machine stability will be reduced with only current/torque control. The feedback of speed signals provides additional challenges such as measurement noise, data transmission, stability etc. If the test bench has mechanical oscillations, this will affect the whole simulation. It can also become cumulative and create further mechanical oscillations, causing instability in the vehicle simulation.

Similar to the torque open-loop interface, the electric machine can be controlled using the current/torque control. Considering the fast response of current control in electric machine, the rotor speed measured in external powertrain and vehicle are at the same step. Therefore, the speed feedback signals will not creates time delay. Parameter errors of machine controller can lead to speed differences between the external powertrain and the vehicle model. As a result, a difference is created in the close-loop co-simulation. These differences will be presented in the next chapter by case study.

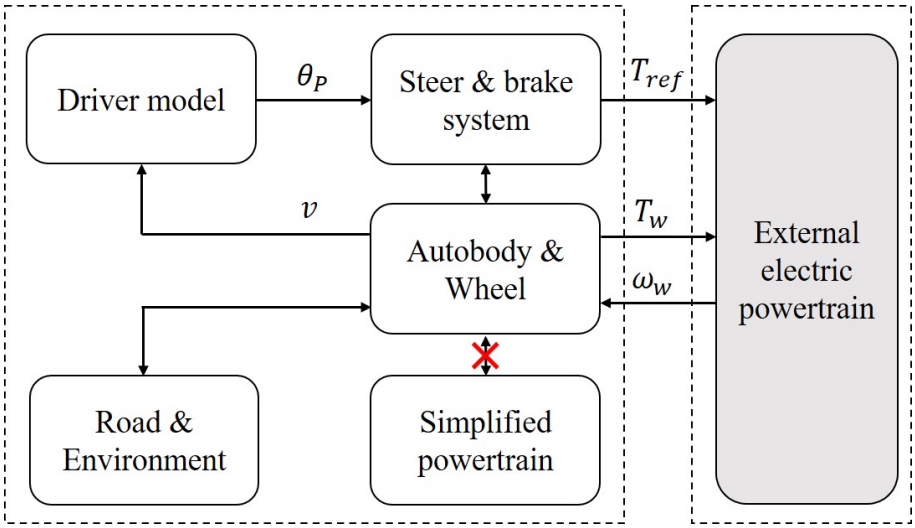

Figure 4.2: Torque close-loop coupling method between vehicle and electric powertrain

4.3 Speed open-loop coupling method

The signal interactions of speed open-loop is shown in Fig.4.3. The load torque T_w into external powertrain is same as torque couplings. While another input is the the wheel speed ω_w instead of the driving torque T_{ref} in torque couplings. In this method, the external powertrain is acting as both follower and observer based on vehicle signals. The output comparison between vehicle model and external powertrain model is the driving torques of each motor/wheel. The vehicle modeling is same as torque couplings, and it runs alone.

Due to the speed inputs, the external powertrain is using the speed controller, as shown in Fig.2.6. The wheel speeds calculated in vehicle model is used as the speed reference ω_w for controlling the electric machine in external powertrain. With the load torque inputs, the actual driving torque T_{ref} of each wheel can be calculated by equation 2.11. Considering the different bandwidth of speed control and current control, i.e., the responsing time of machine controller, there can be a difference in rotor speed between the vehicle model and external powertrain.

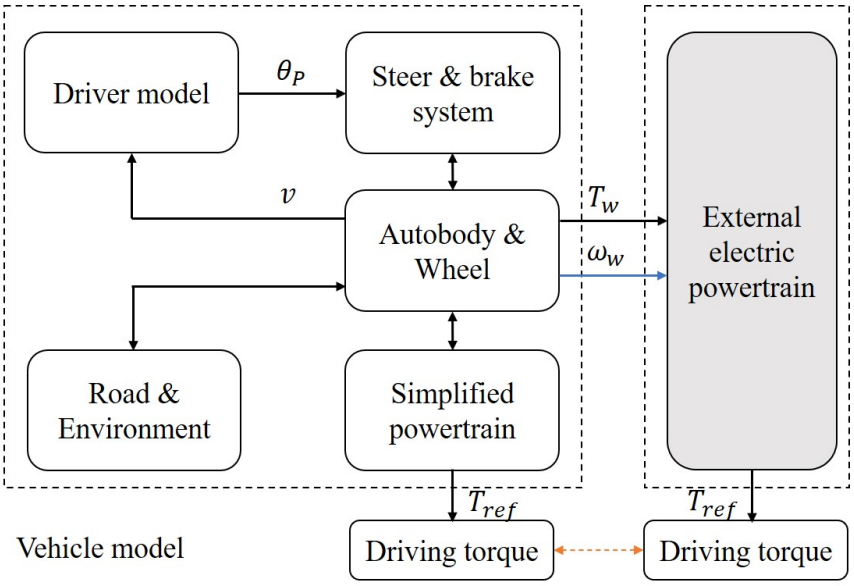

Figure 4.3: Speed open-loop coupling method between vehicle and electric powertrain

4.4 Speed close-loop coupling method

In the speed close-loop interface, as shown in Fig.4.4, the driving torque T_{ref} signals of each rear wheel are feedback to vehicle model for calculating the speed of each wheel. The calculation of wheel speeds are still using the simplified powertrain in vehicle model. The external powertrain is acting as a middle part between vehicle model and its internal simplified powertrain, and it still can be treated as a close-loop simulation.

In this method, the motor speed of external powertrain will be delayed due to its lower control bandwidth, and the synchronization between two models will be effected. However, this method can improve the electric machine stability, especially in real HIL test bench. Several problems can be sovled like speed oscillations, unwanted yaw movement of the vehicle, and large flywheel requirements. Therefore, comparing to torque close-loop coupling, the speed close-loop coupling is more suitable for HIL test cases. Due to the control bandwidth of speed control mode, the torque feedback should be enabled after few seconds. Otherwise, the vehicle will have a loop conflict and cannot be started.

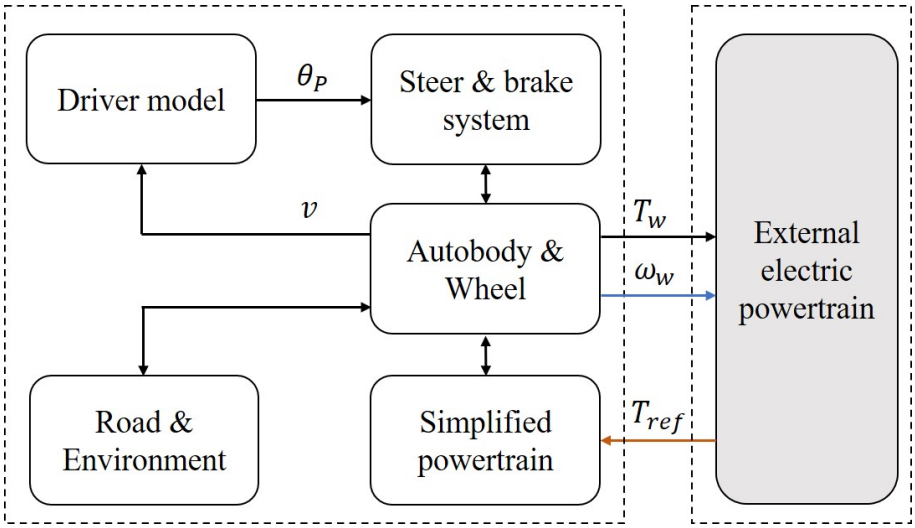

Figure 4.4: Speed close-loop coupling method between vehicle and electric powertrain

4.5 Comparison of coupling methods

The reference torque (from driver) in all cases are ramped up at 0.1s to 50Nm with a low-pass filter (LPF) having a bandwidth of 0.3 rad/s. The vehicle drives on a straight-line trajectory for 5s. The results of four coupling approaches, including wheel speed, electromagnetic torque T_{ref} and load torque T_w, are compared in Fig.4.5 and Fig.4.6. The blue color indicates the results of the open-loop approaches, while the close-loop couplings are represented by orange color.

4.5.1 Torque open-loop & Torque close-loop

Fig.4.5 shows the comparison of torque open-loop and torque close-loop coupling methods. In the first subplot, the slope of wheel speed in close-loop (orange) is higher than open-loop (blue), around 0.4 rad/s^2. It can be explained by observing the electromagnetic torque T_{ref} in the second subplot. Due to the use of LPF in the reference torque generation, it takes roughly 2 seconds for the torque to reach the reference. The electromagnetic torque in both method is the same, and shown as overlapped by the orange solid line in second subplot, owing to the fast current control mode in PMSM (with 1500 kHz bandwidth, as shown in Fig.2.6).

Differences in the load torque between the two coupling methods are visible in second subplot. In open loop coupling (blue dash line), the external powertrain just uses the two torques of vehicle to solve the wheel speed and does not affect the vehicle simulation. While, in close-loop coupling (orange dash line), the wheel speed calculation in vehicle is based on the external powertrain, which means the load torque losses in external powertrain (PMSM efficiency, gearbox losses, etc.) are also involved in close-loop simulation. Therefore, the total load torque in close-loop coupling will lower than open-loop coupling. And these load torque gap leads to dif-

ferent slop of wheel speed. However, the difference of speed and torque are correct, and it means the vehicle simulates under more complex conditions.

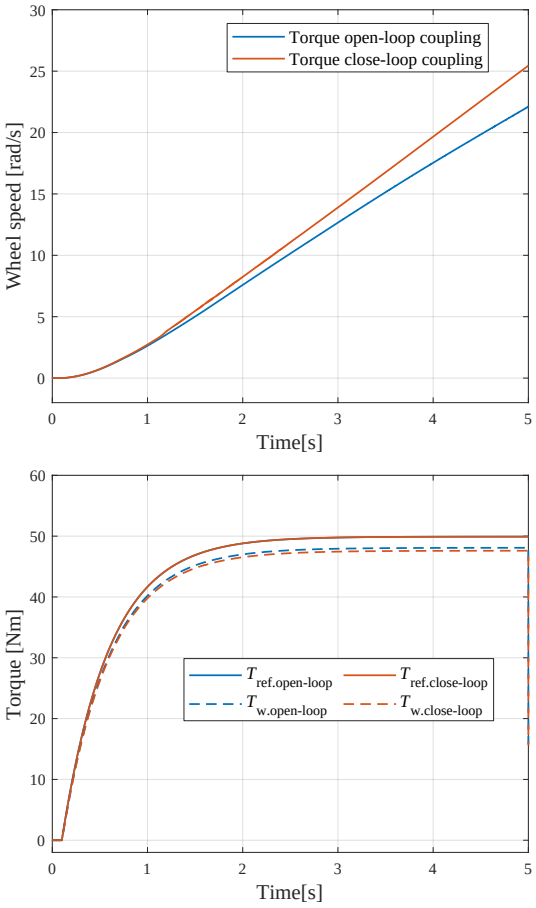

Figure 4.5: Comparison between torque open-loop (blue) and torque close-loop couplings (orange)

4.5.2 Speed open-loop & Speed close-loop

The difference between speed open-loop and speed close-loop interfacing methods is shown in Fig.**??**. The speed coupling performances are similar to torque couplings. In the first subplot, the slope of wheel speed in close-loop (orange) is higher than open-loop (blue), and this slop difference is much higher than torque couplings, almost 3 rad/s^2. This is caused by the high frequency torque oscillations in PMSM, as shown in the second subplot.

Due to the speed control mode of PMSM (with 150 kHz bandwidth in Fig.2.7), the electromagnetic torque in speed open-loop method is always chasing the reference torque instead of equal to that value. Therefore, these torques are not linear and oscillates with high frequency (blue line in second subplot). In the speed close-loop method, the electromagnetic torque also oscillates in high frequency (not shown in figure), and this will make the vehicle model unstable. To overcome this problem,

a low-pass-filter with 1000 kHz bandwidth is inserted between vehicle model and external powertrain.

The filtered electromagnetic torque is shown in the second subplot with orange solid line, and it is higher than the reference torque from driver. Considering the similar load torque losses in external powertrain, the slop of wheel speed in speed close-loop method is much higher than open-loop connections. Furthermore, this speed value is also much higher than torque close-loop method. So, comparing the two close-loop methods, the torque close-loop coupling is more suitable on offline simulations.

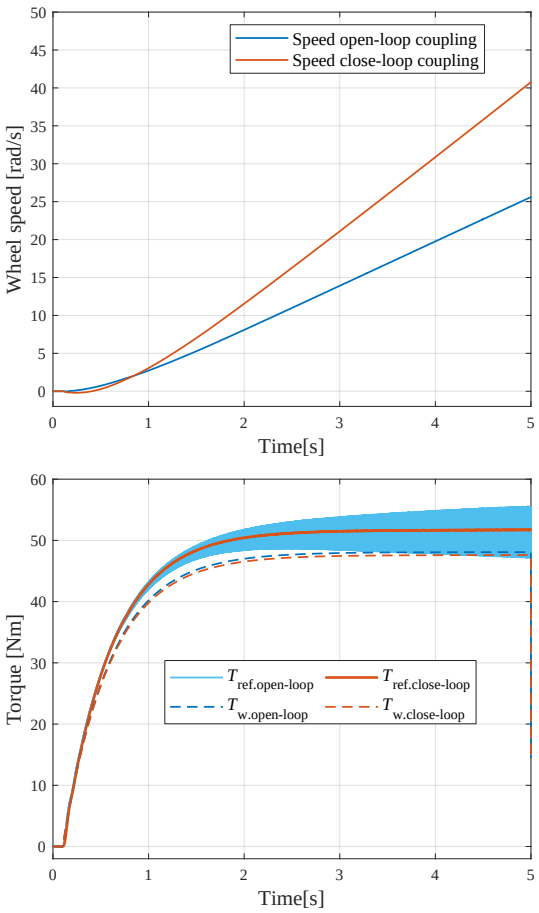

Figure 4.6: Comparison between speed open-loop (blue) and speed close-loop couplings (orange)

5

Results

In this section, the results of four simulated test cases are presented to support the various functionalities of the proposed co-simulation vehicle model. In the first case, the simulation results of two types of electric machines, as described in section II, are compared. Then, the second test case is comparing the co-simulation vehicle model and simplified vehicle model. The third case is study the impacts of drivers behaviors on thermal performance of electric machine and inverter. In the final case, the functionality of vehicle model for wheel anti-slip control validation based on three driving conditions are introduced.

5.1 Case 1: Comparison between incremental and apparent inductance PMSM

In this case, only electric machines are simulated. Fig5.1 shows the results of motor speed and torque in two types of electric machines. PMSM 1 and PMSM 2 are the incremental inductance machine (2.1 2.2) and apparent inductance machine(2.6 2.7), respectively. In the first subplot, the slop of rotor speed in PMSM 1 is higher than PMSM 2. The speed dynamics can be explained by observing the electromagnetic torque in the second subplot.

The reference torque in two machines is 20 Nm during simulation, as shown by the blank line in second subplot. And the load torque is 15Nm in both machine, which is not shown in this plot. Due to the different inductance mode in equation 2.5 and 2.8, the output torques will be different as shown in the second subplot. However, the electromagnetic torque of each machine mode is not equal to the reference torque (black line). This is because the different models of PMSM and machine controller. Each PMSM model is using the dynamic FEM parameters of flux linkage and inductance, which makes it simulating in a dynamic condition in addition to a constant parameters condition. While the parameters of each machine controller is the same fixed parameter model. Therefore, the electrical torque after controller will always have some error. And this will lead to the torque oscillation at beginning, as shown in the second subplot.

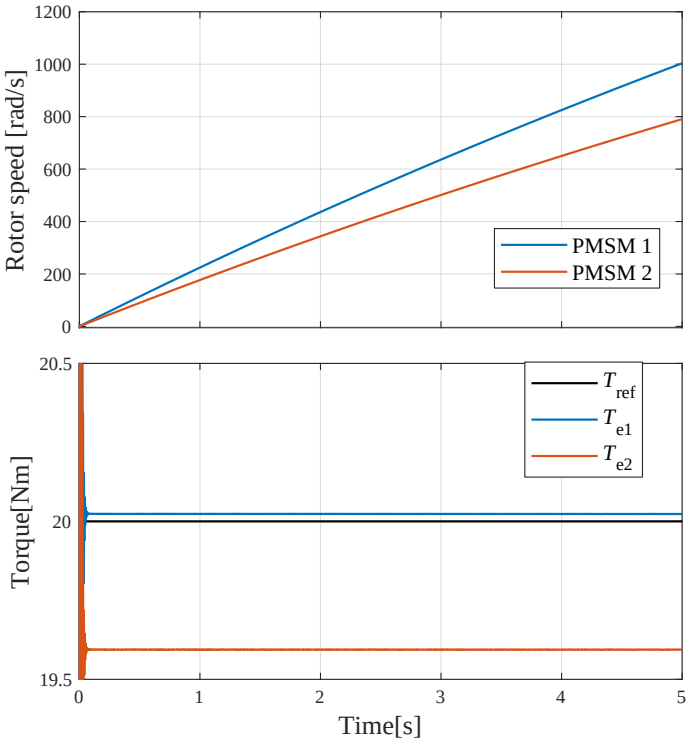

Figure 5.1: Rotor speed and torque comparison in two PMSM model

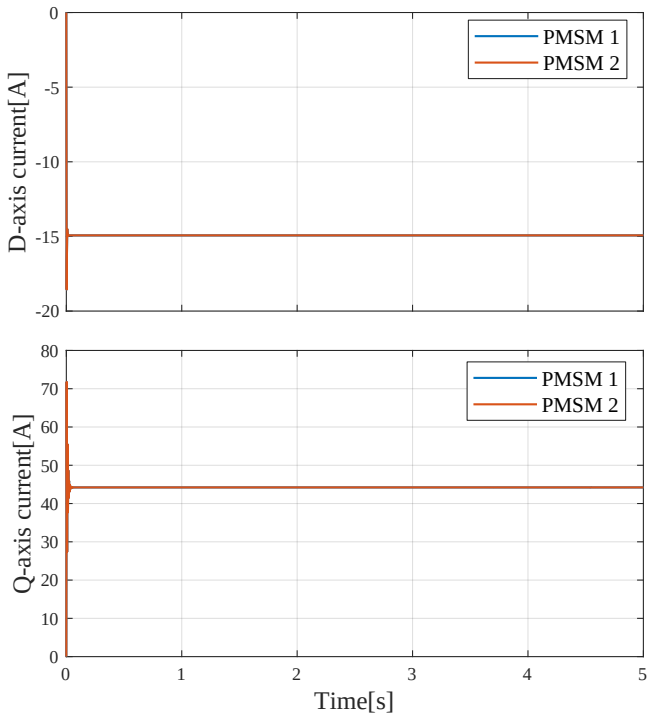

Figure 5.2: d&q currents comparison in two PMSM model

Fig.5.2 shows the d&q currents in two PMSM, each machine is using the current

control and maximum torque per ampere (MTPA) control strategy. The look-up table for d&q reference currents in both machines are same, which means the actual d&q currents will be the same, as shown by the overlapped line orange in each subplot. The current oscillation at the beginning is owing to the parameter errors between PMSM model and current reference values. Moreover, all other test cases are using the PMSM 1, i.e., the flux linkage PMSM.

5.2 Case 2: Comparison between simplified vehicle model and co-simulation vehicle model

In this case, the results of two co-simulation approaches of vehicle model are presented. In the first model, the external electric powertrain relates to simplified vehicle equations 3.1 to 3.10. Only longitudinal motion of the vehicle is considered, and it is very difficult to model driver behaviors, road and environment conditions. The second method uses the external electric powertrain (section II) and detailed vehicle model (section III) based on torque close-loop coupling method (section III).

The reference torque rises to 50Nm at 0.2s and drops down as the vehicle speed reaches 50km/h with a low-pass filter (LPF) bandwidth of 0.3 rad/s. In addition, the vehicle moves on a straight trajectory during the simulation. The results of two co-simulation approaches, including vehicle speed, rotor speed, electromagnetic torque and load torque, and dq axis currents, are compared in Fig.**??**. The subscript "1" and blue color indicates the results of the first approach, and the second one is represented by the subscript "2" and orange color.

In the first two subplots, the slope of vehicle and motor speeds increase at the beginning and reaches a constant value. The difference between two speeds is based on the unit transformation and gearbox ratio. The speed dynamics can be explained by observing the electromagnetic torque in the third subplot. Due to the use of LPF in the reference torque generation and FOC, it takes approximate 0.7 second for the torque to reach the reference. When the reference torque is removed and electromagnetic torque decreases, the vehicle starts decelerating, due to the same LPF, it delays roughly 0.7 second to decrease the driving torque when vehicle reaches 50km/h. Therefore, the final speed values are over 50km/h. However, the deceleration is much slower as no braking torque is applied and only the wheel resistance torque helps to stop the vehicle. It can also be observed that the load torque is smaller than the electromagnetic torque, as the difference is used to accelerate the combined rotational inertia of electric machine, gearbox and wheels. The d&q currents in subplot four follow the electromagnetic torque. Maximum torque per Ampere (MTPA) is used to select the current references.

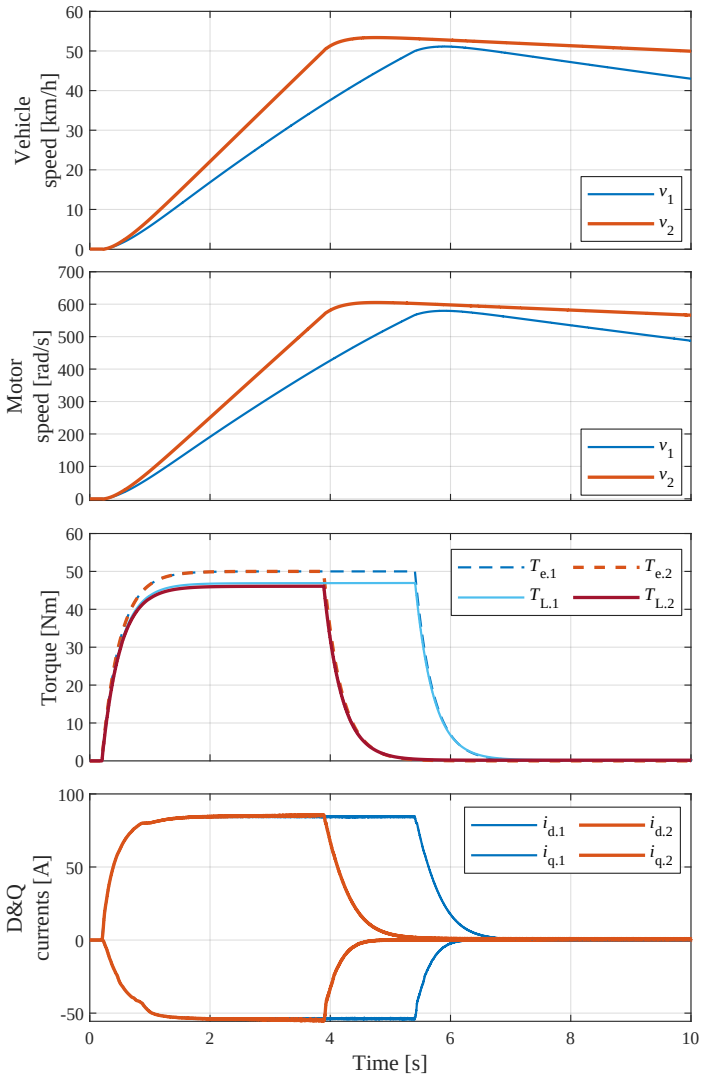

Figure 5.3: Simulation results showing comparation of two co-simulation vehicle models

Fig.5.4 shows the power losses and thermodynamics of PMSM and inverter based on the same drive conditions. The sum of the copper and iron losses of the motor is shown in the first subplot. At the beginning, the copper losses dominate, as the sum coincides with the torque curve. Later, as the speed increases, the iron losses become noticeable, and the sum follows the speed curve. The PMSM winding temperatures shown in the second subplot start at 65°C, which is the ambient temperature in motor LPTN. At the beginning, the slope of the winding temperature increases more rapidly, in line with the increase in motor losses. As the speed decreases, the total losses decrease, mainly iron losses. As a result, the winding temperature does not increase further because the iron losses in the core are dissipated more efficiently. The conduction losses of the MOSFETs are proportional to the square of the current, while the switching losses are proportional to the dc-link voltage and current [23]. Since the dc-link voltage is constant in the simulation, the total inverter losses in subfigure three are proportional to the current. The junction temperature of the

MOSFET in the last subplot is driven by the inverter losses. It starts at 25°C, due to the temperature setting of the inverter coolant.

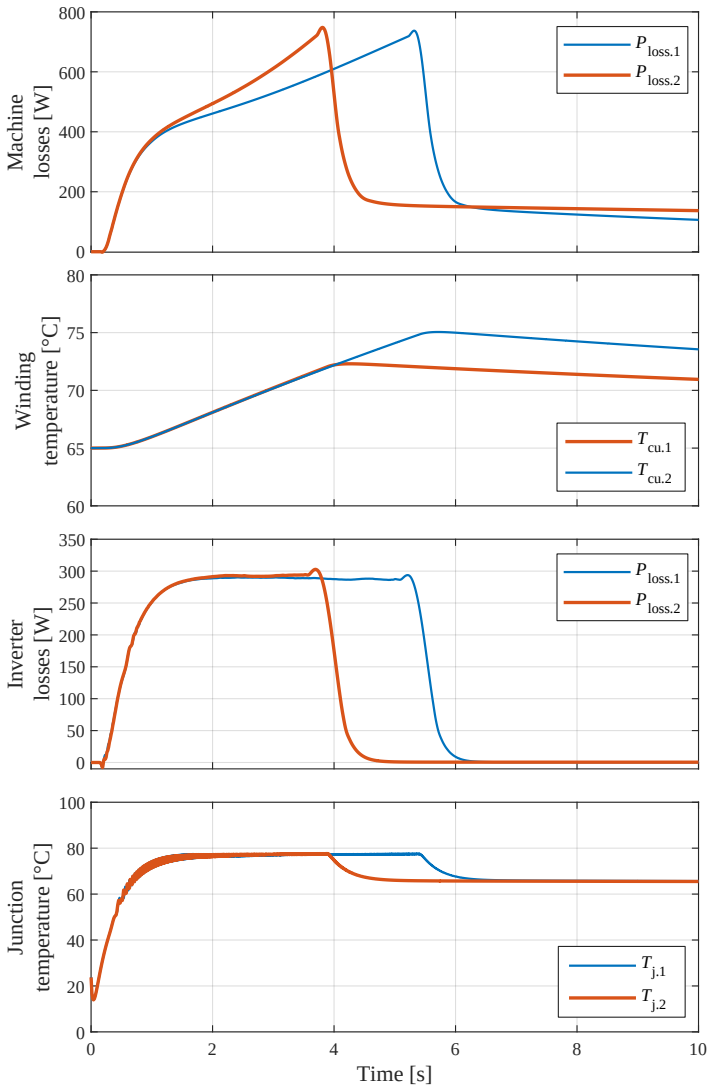

Figure 5.4: Thermal and power losses of two co-simulation vehicle models

The difference between the results of the two methods is visible in Fig.5.3 and 5.4. In the first method the vehicle speed lags the second method, even though the electromagnetic torque is the same between the two simulations. This is due to the different methods used to calculate the load torque, which is slightly higher in the first method. The d&q currents are almost identical in both methods. The total losses of the motor start to diverge with the speed difference, as they depend on both torque and speed. The winding temperature is the same in both methods, as the copper losses should be the same. The inverter losses are the same because they are mainly current dependent. The temperature of the junctions is therefore the same in both methods. There is a difference of five to seven seconds, which is caused by the common simulation method.

5.3 Case 3: Thermal behaviors during different driver models

In this case, the road and environment model shown in Fig.3.5 and the three driver models shown in Fig.3.2 were used. A distance-based driving task was used and the results of the first lap (2.2 km) are shown in Fig.5.5. The values of x-axes in all subplots are distance instead of time. As the vehicle was driven in cycles, it did not come to a complete stop at the end of the simulation cycle. Three subplots are shown: vehicle speed, electromagnetic torque, and elapsed time. The red, black and blue curves represent the aggressive, normal and defensive driver models respectively. All drivers have a maximum speed of 150km/h, only the acceleration and deceleration speeds are different.

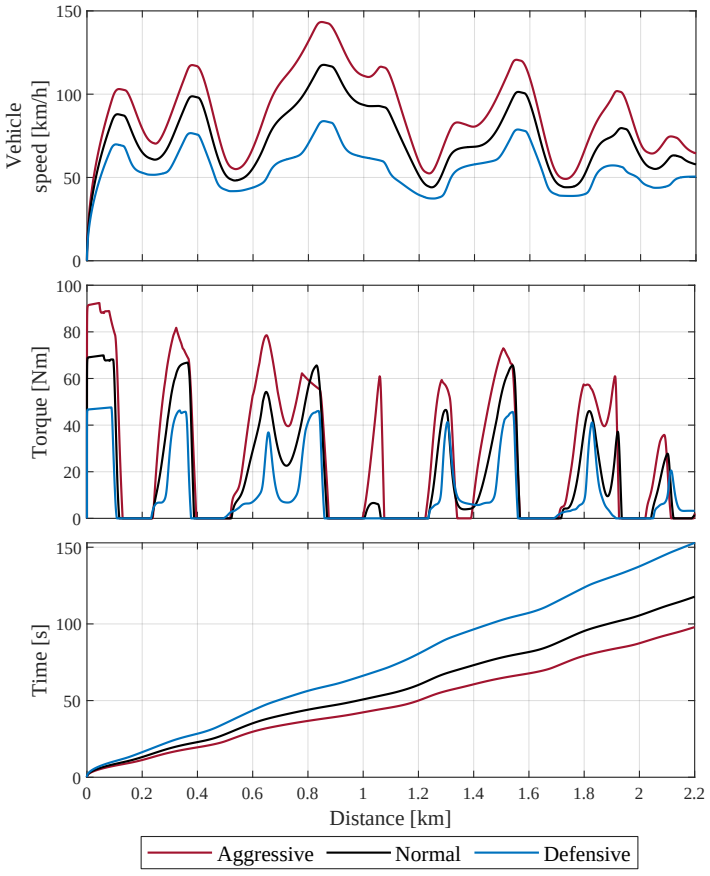

Figure 5.5: Simulation results showing comparison of three driver models

The three different driver models lead to three different driving performances, as shown in the subplots for the vehicle speeds. The local minima and maxima in the speed diagram correspond to tight corners and straight sections respectively. The electromagnetic torque is determined by the driver's acceleration requirements and is almost zero when the vehicle is decelerating. The elapsed time in the third

subplot is inversely proportional to the average vehicle speed. The difference in speed between aggressive and defensive drivers ranges between 20% and 50%. During acceleration, the effect of the driver model on EM torque is more pronounced compared to deceleration. The aggressive driver has the highest average speed.

Fig.5.6 shows the machine losses, winding temperatures, inverter losses and junction temperatures based on the three driving habits. The initial temperatures of winding and inverter are same as case 2. This thermal and power losses shows similar behaviours to that observed in the previous case. There is a 30% difference in the maximum winding temperature between the aggressive and defensive drivers. Similarly, the junction temperature varies by 25%, but it varies much faster due to the much smaller thermal capacitance.

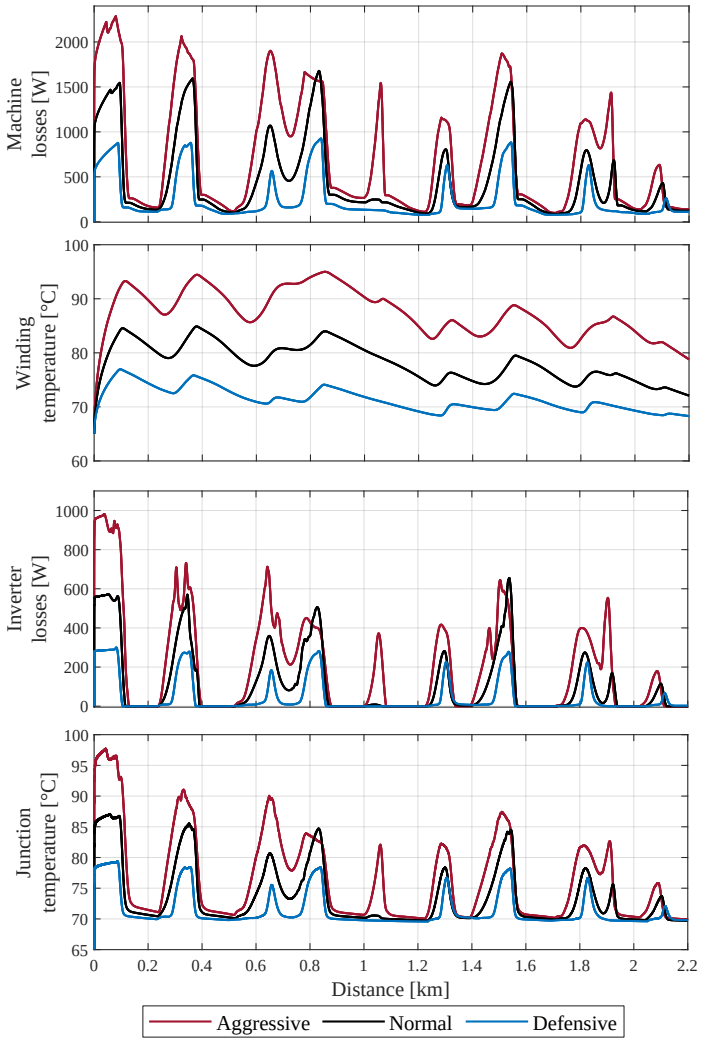

Figure 5.6: Thermal and power losses of PMSM and inverter based on three driving habits

5.4 Case 4: Wheel slip control test case

In this case, the reference torque is defined as a constant value 104Nm on each rear wheel and the driver signal is disconnected. The parameters of road and environment are presented in 3.6. The vehicle starts on normal road surface and accelerates into the ice road (friction coefficient μ=0.2) at t=4.125s or 30m. The results of vehicle with or without controller, including vehicle speed, wheel speed, slip ratio, and driving torque and load torque, are compared in Fig.5.7. The blue lines indicate the results with controller, while the orange lines are vehicle without controller.

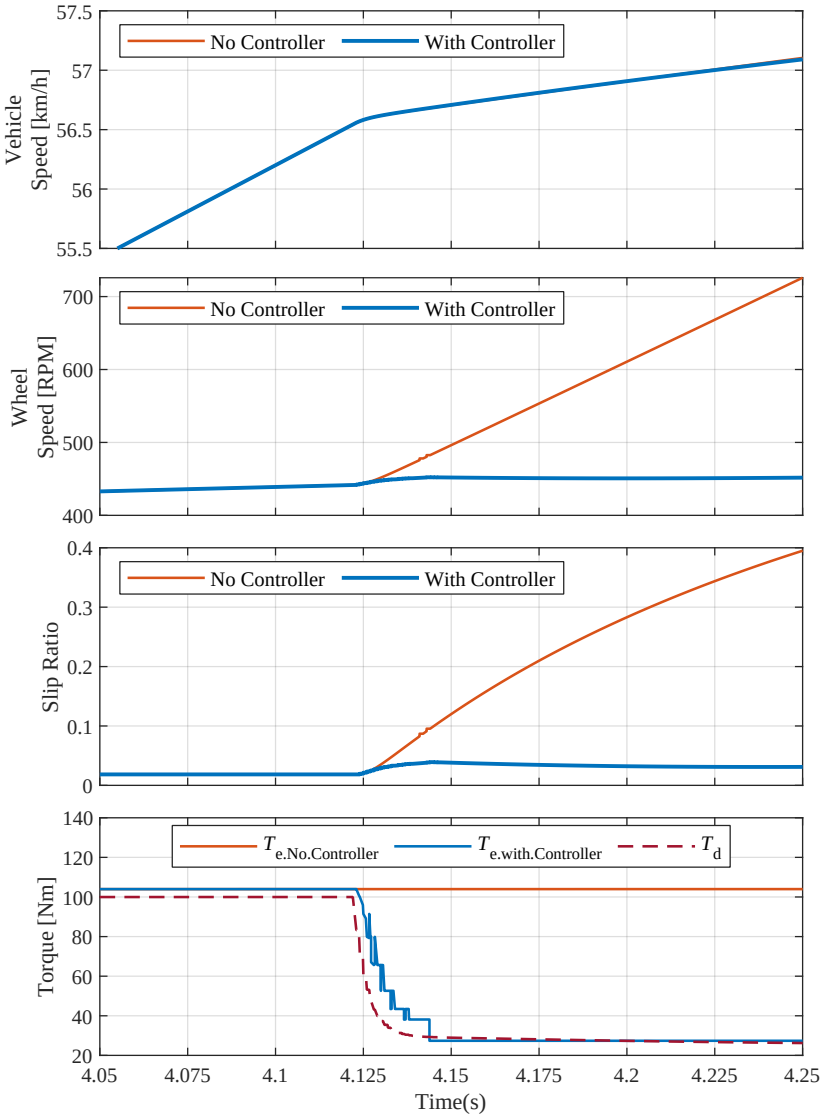

Figure 5.7: Vehicle dynamics when driving in ice road, comparison between vehicles with and without controller

In Fig.5.7, the first subplot shows the vehicle speed with and without controller. Due to the short measurement time, only 0.2s, vehicle vehicle does not change as

quickly as wheel speed, which results in an overlap of two vehicle speeds, and for long period, this two values are different. But it is enough for observing the controller performance. In the second subplot, The wheel speed (orange line) of the vehicle without controller increases significantly, while the wheel of the vehicle with controller (blue line) changes slightly. Considering the same vehicle speeds in first subplot and equation3.17, the slip ratio in no controller vehicle will increase seriously, while the slip ratio in vehicle with controller still can close to zero, as shown in the third subplot.

These can be explained by observing the electromagnetic torques and load torque in the fourth subplot. In both vehicle, the driving torque before controller remain constant at 104Nm. When the load torque is reduced from 100Nm to 24Nm at slip road and the electromagnetic torques keep constant, the wheel starts accelerating. And this acceleration is much faster without controller since the controller can reduce the electromagnetic torque from 104Nm to 28Nm constantly. It can also be observed that the load torque is smaller than the electromagnetic torque, as the difference is used to accelerate the electric machine and wheel.

6

Conclusion

This paper presents a high-fidelity full-vehicle modeling method that uses two dedicated simulation tools to model the vehicle and the electric powertrain separately. The main contribution of this thesis is the introduction of a multi-functional vehicle platform consists of thermal unit and wheel slip control unit. This approach is not limited to improve the accuracy by co-simulation, but also aims at developing a high-fidelity platform for online fault diagnosis and efficiency optimization on the next generation of electric vehicle.

The advantages and disadvantages of four different coupling methods are presented and verified by analyzing the electric powertrain model. The purpose of the open-loop simulation is to verify the feasibility of platform docking. The closed-loop torque simulation has a higher accuracy and is more suitable for offline simulation, while the closed-loop speed simulation is more suitable for HIL test bench. In case 1 study, different electric machine models affect the accuracy of the powertrain system. For offline platform simulations the effect is not significant, but for HIL platforms a detailed model comparison is necessary. In case 2 and case 3, the two proposed co-simulation method was compared. It was observed that co-simulation using simplified vehicle model leads to an underestimation of the vehicle and powertrain system. Furthermore, the simulation of driver behaviour and road conditions requires the use of specialised simulation tools (like CarMaker) to model the vehicle when performing co-simulation. Furthermore, the use of a common simulation environment for vehicle and electric powertrain modelling makes co-simulation simpler by reducing the complexity of the design model interface. Simplified lumped parameter thermal networks are used to model the heat dissipation of PMSM and inverter. Three drive models were used together with distance-based drive tasks to investigate winding and junction temperatures. Simulation results show a maximum temperature difference of 30% and 25% for the motor windings and semiconductor junctions due to the different drive models. Although an aggressive drive leads to higher temperatures, the duration of the temperature cycles is relatively short. In case 4, the simulations of wheel slip control strategy during acceleration is presented. With wheel slip control, the traction wheel dynamics can be detected and managed during extreme conditions based on the detailed electric powertrain system.

Overall, the platform can satisfy various requirements quite well. Therefore, demonstrating the capability in both simulation and multi-function verification while using high fidelity co-simulation platform. This research also paves the way for the next step real-time simulation and hardware-in-the-loop test bench. Fig.**??** shows the

already established back-to-back test bench.

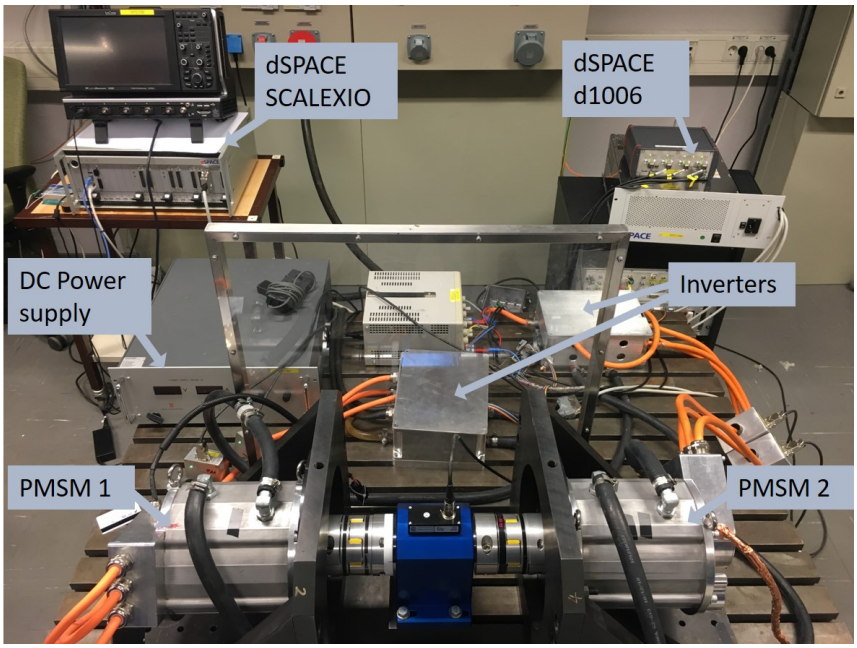

Figure 6.1: The setup of back-to-back machine test bench

The test bench shown in Fig.6.1 consists of two identical electric machines powered via two voltage source converters (VSCs). The DC links of the two VSCs are connected to form a back-to-back configuration so that higher powers can be tested with lower power requirements on DC power source. The two machines are mechanically connected with a torque transducer. The controller of each machine is implemented in dSPACE real-time processor d1006. The diagram shows "PMSM 1" for the traction machine and "PMSM 2" for the load machine.

Bibliography

[1] M. Galea, C. Gerada, T. Raminosoa and P. Wheeler, "A Thermal Improvement Technique for the Phase Windings of Electrical Machines," in IEEE Transactions on Industry Applications, vol. 48, no. 1, pp. 79-87, Jan.-Feb. 2012, doi: 10.1109/TIA.2011.2175470.

[2] W. Cao, B. C. Mecrow, G. J. Atkinson, J. W. Bennett and D. J. Atkinson, "Overview of Electric Motor Technologies Used for More Electric Aircraft (MEA)," IEEE Transactions on Industrial Electronics, 55(9), 3300-3306.

[3] C. Gerada and K. J. Bradley, "Integrated PM Machine Design for an Aircraft EMA," IEEE Transactions on Industrial Electronics, 55(9), 3300-3306, Sept. 2008

[4] P. H. Nguyen, E. Hoang and M. Gabsi, "Performance Synthesis of Permanent-Magnet Synchronous Machines During the Driving Cycle of a Hybrid Electric Vehicle," in IEEE Transactions on Vehicular Technology, vol. 60, no. 5, pp. 1991-1998, Jun 2011, doi: 10.1109/TVT.2011.2118776.

[5] S. Dixit et al., "Trajectory Planning for Autonomous High-Speed Overtaking in Structured Environments Using Robust MPC," in IEEE Transactions on Intelligent Transportation Systems, vol. 21, no. 6, pp. 2310-2323, June 2020, doi: 10.1109/TITS.2019.2916354.

[6] X. Zhang, D. G?hlich and J. Li, "Energy-Efficient Toque Allocation Design of Traction and Regenerative Braking for Distributed Drive Electric Vehicles," in IEEE Transactions on Vehicular Technology, vol. 67, no. 1, pp. 285-295, Jan. 2018, doi: 10.1109/TVT.2017.2731525.

[7] T. Brezina, Z. Hadas and J. Vetiska, "Using of Co-simulation ADAMS-SIMULINK for development of mechatronic systems," 14th International Conference Mechatronika, Trencianske Teplice, 2011, pp. 59-64, doi: 10.1109/MECHATRON.2011.5961080.

[8] V. R. Aparow, A. Choudary, G. Kulandaivelu, T. Webster, J. Dauwels and N. d. Boer, "A Comprehensive Simulation Platform for Testing Autonomous Vehicles in 3D Virtual Environment," 2019 IEEE 5th International Conference on Mechatronics System and Robots (ICMSR), 2019, pp. 115-119, doi: 10.1109/ICMSR.2019.8835477.

[9] B. Chen, S. A. Evangelou and R. Lot, "Fuel Efficiency Optimization Methodologies for Series Hybrid Electric Vehicles," 2018 IEEE Vehicle Power and Propulsion Conference (VPPC), 2018, pp. 1-6, doi: 10.1109/VPPC.2018.8604991.

[10] B. S. Umesh and K. Sivakumar, "Multilevel Inverter Scheme for Performance Improvement of Pole-Phase-Modulated Multiphase Induction Motor Drive," in

IEEE Transactions on Industrial Electronics, vol. 63, no. 4, pp. 2036-2043, April 2016, doi: 10.1109/T IE.2015.2506623.

[11] R. Azar, F. Udrea, W. T. Ng, F. Dawson, W. Findlay and P. Waind, "The Current Sharing Optimization of Paralleled IGBTs in a Power Module Tile Using a PSpice Frequency Dependent Impedance Model," in IEEE Transactions on Power Electronics, vol. 23, no. 1, pp. 206-217, Jan. 2008, doi: 10.1109/TPEL.2007.909182.

[12] S. Rebiai, H. Bahouh and S. Sahli, "2-D simulation of dual frequency capacitively coupled helium plasma, using COMSOL multiphysics," in IEEE Transactions on Dielectrics and Electrical Insulation, vol. 20, no. 5, pp. 1616-1624, Oct. 2013, doi: 10.1109/TDEI.2013.6633691.

[13] T. V. Frandsen et al., "Motor Integrated Permanent Magnet Gear in a Battery Electrical Vehicle," IEEE Transactions on Industry Applications, 51 (2), 1516-1525

[14] N. R. Patel, V. A. Shah and M. M. Lokhande, "A Novel Approach to the Design and Development of 12/15 Radial Field C-Core Switched Reluctance Motor for Implementation in Electric Vehicle Application," in IEEE Transactions on Vehicular Technology, vol. 67, no. 9, pp. 8031-8040, Sept. 2018, doi: 10.1109/TVT.2018.2839695.

[15] L. Xu, Y. Zhang and X. Wen, "Multioperational Modes and Control Strategies of Dual-Mechanical-Port Machine for Hybrid Electrical Vehicles," IEEE Transactions on Industry Applications, 45(2),747-755

[16] A. Emadi, S. Onoda , "PSIM based modeling of auto-motive power systems: electric, conventional, and hybrid electric vehicles," in IEEE Transactions on Vehicular Technology, vol. 53, no. 2, pp. 390-400, March 2004, doi: 10.1109/TVT.2004.823500.

[17] Q. Chen, G. Liu, W. Gong and W. Zhao, "A New Fault-Tolerant Permanent-Magnet Machine for Electric Vehicle Applications," in IEEE Transactions on Magnetics, vol. 47, no. 10, pp. 4183-4186, Oct. 2011, doi: 10.1109/TMAG.2011.2146238.

[18] S. Fang, Q. Liu, H. Lin and S. L. Ho, "A Novel Flux-Weakening Control Strategy for Permanent-Magnet Actuator of Vacuum Circuit Breaker," in IEEE Transactions on Industrial Electronics, vol. 63, no. 4, pp. 2275-2283, April 2016, doi: 10.1109/TIE.2015.2500182.

[19] Abdelrahman, A. S., Algarny, K. S., Youssef, M. Z. (2018). A novel platform for power-train modeling of electric cars with experimental validation using realtime hardware-in-the-loop (HIL): A case study of gm second generation Chevrolet volt. IEEE Transactions on Power Electronics, 33(11), 9762-9771.

[20] K. Ahn, A. E. Bayrak and P. Y. Papalambros, "Electric Vehicle Design Optimization: Integration of a High-Fidelity Interior-Permanent-Magnet Motor Model," in IEEE Transactions on Vehicular Technology, vol. 64, no. 9, pp. 3870-3877, Sept. 2015, doi: 10.1109/TVT.2014.2363144.

[21] K. Ma, M. Liserre, F. Blaabjerg and T. Kerekes, "Thermal Loading and Lifetime Estimation for Power Device Considering Mission Profiles in Wind Power Converter," in IEEE Transactions on Power Electronics, vol. 30, no. 2, pp. 590-602, Feb. 2015, doi: 10.1109/TPEL.2014.2312335.

[22] S. Dusmez, H. Duran and B. Akin, "Remaining Useful Lifetime Estimation for Thermally Stressed Power MOSFETs Based on on-State Resistance Variation," IEEE Transactions on Industry Applications, 52(3), 2554-2563.

[23] P. Cygan and J. R. Laghari, "Models for insulation aging under electrical and thermal multistress," in IEEE Transactions on Electrical Insulation, vol. 25, no. 5, pp. 923-934, Oct. 1990, doi: 10.1109/14.59867.

[24] D2.1 Preliminary design of modular drivetrain system, related Task 2.1 of WP2, submitted on April 2018. Nimananda Sharma and Yujing Liu, Chalmers University of Technology.

[25] S. Tenner, S. Gunther, and W. Hofmann, “Loss minimization of electric drive systems using a dc/dc converter and an optimized battery voltage in automotive applications,” in Proc. IEEE VPPC, 2011, pp. 1–7.

[26] K. Gulez, A. A. Adam and H. Pastaci, "Torque Ripple and EMI Noise Minimization in PMSM Using Active Filter Topology and Field-Oriented Control," IEEE Transactions on Industrial Electronics, 55(1), 251-257.

[27] Junfei Tang et al, ‘Design and Control of Electrically Excited Synchronous Machines for Vehicle Applications", Chalmers University of Technology, Sweden, 2021, ISBN: 9789179054663.

[28] N. Bracikowski, M. Hecquet, P. Brochet and S. V. Shirinskii, "Multiphysics Modeling of a Permanent Magnet Synchronous Machine by Using Lumped Models," IEEE Transactions on Industrial Electronics,59(6), 2426-2437.

CHALMERS
UNIVERSITY OF TECHNOLOGY